Title

Antimicrobial Bioresorbable Mg–Zn–Ca Alloy for Bone Repair in a Comparison Study with Mg–Zn–Sr Alloy and Pure Mg

Journal

ACS Biomaterials Science & Engineering, 6(1)

ISSN

2373-9878

Authors

Zhang, Chaoxing
Lin, Jiajia
Nguyen, Nhu-Y Thi
et al.

Publication Date

2020-01-13

DOI

10.1021/acsbiomaterials.9b00903

Peer reviewed

HHS Public Access

Author manuscript

ACS Biomater Sci Eng. Author manuscript; available in PMC 2021 June 22.

Published in final edited form as:

ACS Biomater Sci Eng. 2020 January 13; 6(1): 517–538. doi:10.1021/acsbiomaterials.9b00903.

Antimicrobial Bioresorbable Mg–Zn–Ca Alloy for Bone Repair in a Comparison Study with Mg–Zn–Sr Alloy and Pure Mg

Chaoxing Zhang[†,‡], **Jiajia Lin**[†,‡], **Nhu-Y Thi Nguyen**[§], **Yuxing Guo**[‖], **Changlu Xu**[†,‡], **Catherine Seo**[‡], **Edgar Villafana**[‡], **Hector Jimenez**[‡], **Yang Chai**[‖], **Renguo Guan**[⊥], **Huinan Liu**[*,†,‡,§,#,□]

[†]Materials Science and Engineering Program, University of California at Riverside, 900 University Avenue, Riverside, California 92521, United States

[‡]Department of Bioengineering, University of California at Riverside, 900 University Avenue, Riverside, California 92521, United States

[§]Microbiology Graduate Program, University of California at Riverside, 900 University Avenue, Riverside, California 92521, United States

[‖]Center for Craniofacial Molecular Biology, Herman Ostrow School of Dentistry, University of Southern California, Los Angeles, California 90007, United States

[⊥]School of Materials Science and Engineering, Northeastern University, Shenyang 110819, China

[#]Biomedical Sciences Program, School of Medicine, University of California at Riverside, 900 University Avenue, Riverside, California 92521, United States

[□]Stem Cell Center, University of California at Riverside, 900 University Avenue, Riverside, California 92521, United States

Abstract

Magnesium–zinc–calcium (Mg–Zn–Ca) alloys have attracted increasing attention for biomedical implant applications, especially for bone repair, because of their biocompatibility, biodegradability, and similar mechanical properties to human bone. The objectives of this study were to characterize Mg–2 wt % Zn–0.5 wt % Ca (named ZC21) alloy pins microstructurally and mechanically, and determine their degradation and interactions with host cells and pathogenic bacteria in vitro and in vivo in comparison with the previously studied Mg–4 wt % Zn–1 wt % strontium (named ZSr41) alloy and Mg control. Specifically, the in vitro degradation and cytocompatibility of ZC21 pins with bone marrow derived mesenchymal stem cells (BMSCs) were investigated using both direct culture and direct exposure culture methods. The adhesion density of BMSCs on ZC21 pins (i.e., direct contact) was significantly higher than on pure Mg pins in both in vitro culture methods; the cell adhesion density around ZC21 pins (i.e., indirect contact) was similar to the cell-only positive control in both in vitro culture methods. Interestingly, ZC21 showed a higher daily degradation rate, crack width and crack area ratio in the direct exposure

[*]**Corresponding Author:** huinan.liu@ucr.edu.

The authors declare no competing financial interest.

culture than in the direct culture, suggesting different culture methods did affect its in vitro degradation behaviors. When cultured with Gram-positive bacteria methicillin-resistant *Staphylococcus aureus* (MRSA), ZC21 reduced bacterial adhesion on the surface more significantly than that of ZSr41 and Mg. The in vivo degradation and biocompatibility of the ZC21 pins for bone regeneration were studied in a mouse femoral defect model. The in vivo degradation rate of ZC21 pins was much slower than that of ZSr41 alloy and Mg control pins. After 12 weeks of implantation in vivo, the ZC21 group showed the shortest gap at the femoral defect, indicating that ZC21 pins promoted osteogenesis and bone healing more than ZSr41 and Mg control pins. Overall, the ZC21 alloy is promising for bone repair, while providing antibacterial activities, and should be further studied toward clinical translation.

Graphical Abstract

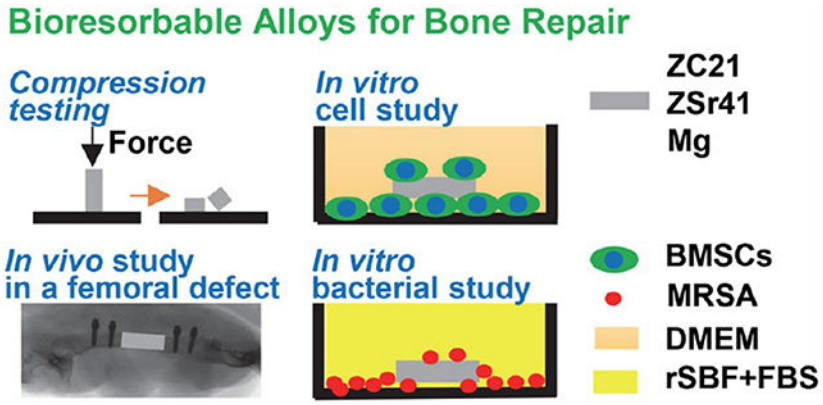

Keywords

biodegradable alloys; magnesium–zinc–calcium (Mg–Zn–Ca); magnesium–zinc–strontium (Mg–Zn–Sr); cytocompatibility with bone marrow derived mesenchymal stem cells (BMSCs); antimicrobial properties; methicillin-resistant Staphylococcus aureus (MRSA); degradation; biocompatibility; mouse femoral defect model in vivo; bioresorbable pins and wires for medical implants

1. INTRODUCTION

Magnesium (Mg) and its alloys have emerged as a new class of bioresorbable materials that are promising for orthopedic and craniofacial implant applications. For example, Mg alloys could be used as internal fixation devices (IFDs) for repairing bone fractures, to replace current standard IFDs made of titanium (Ti) alloys or stainless steels. Mg alloys provide similar mechanical properties to human bone,[1] support bone growth and potentially address the stress-shielding issues associated with Ti alloys and cobalt–chromium (Co–Cr) alloys.[2–8] Mg naturally degrades in physiological fluids by reacting with water, and the degradation products can be metabolized effectively by human body, which eliminates the need for a secondary surgery for implant removal after the tissue has healed.[9–11] Unfortunately, pure Mg degrades too rapidly to be directly used for orthopedic implants, because rapid degradation causes a sharp increase of local pH, fast accumulation of hydrogen gas (H_2)

bubbles, and premature loss of mechanical strength.[2,9,12,13] Thus, it is critical to control and improve the degradation rate of Mg for successful clinical translations. Adding alloying elements to Mg has been extensively explored to slow Mg degradation and H_2 evolution.[14,15]

Selecting suitable alloying elements is critical to the mechanical properties, degradation behaviors, and biological properties of Mg-based alloys, because alloying elements and compositions have crucial effects on the microstructure, phase distribution, and biocompatibility of Mg-based alloys.[14,16,17] Metallic alloying elements, such as aluminum (Al) and yttrium (Y), are widely used to improve the corrosion resistance and the mechanical strength of Mg,[18] but their biocompatibility poses a serious concern. Therefore, development of Mg-based alloys with elements that are naturally present in the human body, such as zinc (Zn), calcium (Ca), and strontium (Sr), have attracted increasing interest for medical implant applications.[8,12,19–29] Zn is involved in over 300 enzymatic processes in the human body.[30] The addition of Zn as an alloying element in Mg could reduce grain size,[31] enhance corrosion resistance, provide solid solution and aging strengthening,[14] and improve tensile and creep strength.[32] As reported, the addition of 1–4 wt % Zn in Mg–Zn alloys increased the ultimate tensile strength and the alloy elongation significantly.[33] Therefore, the biocompatibility and corrosion resistance of Mg alloyed with 1–4 wt % Zn have been widely studied in vitro and in vivo.[12,26–28,32–35] Mg–Zn alloys with low Zn content can be further modified by adding a third alloying element, such as Ca.[16,29,36] Ca is a major component of bone and is essential for a variety of cellular functions.[16] Ca also shows a great microstructure-refining effect on Mg alloys.[14] As reported, adding 0.5–1.0 wt % Ca reduced the grain size of Mg alloys.[37] However, the addition of larger amounts of Ca (>1.0 wt %) accelerated the degradation rates of Mg alloys. Therefore, the optimal composition of Ca in Mg alloys should be less than (⩽) 1.0 wt %.[38,39]

In our previous study, as-cast Mg–2 wt % Zn–0.5 wt % Ca (named ZC21) alloy plates showed the best collective properties, including degradation properties and cytocompatibility with bone marrow derived mesenchymal stem cells (BMSCs), among four tested Mg–*x*Zn–0.5 wt % Ca (x = 0.5, 1.0, 2.0, 4.0 wt %) alloy plates using the direct culture method in vitro.[28] Therefore, the ZC21 alloy was selected based on the previous results and fabricated into the form of wires (or pins) for further studies toward clinical translation. The objectives of this study are to determine the degradation of ZC21 alloy pins, and their interactions with host cells and pathogenic bacteria in vitro and in vivo in comparison with the previously studied Mg–4 wt % Zn–1 wt % strontium (named ZSr41) alloy and Mg control. Specifically, the in vitro degradation and cytocompatibility of ZC21 pins with BMSCs in Dulbecco's modified Eagle medium (DMEM) were studied using both direct culture and direct exposure culture methods.[40] The direct culture method is suitable for evaluating attachment of directly seeded cells on the biomaterial surface, while the direct exposure culture method allows us to study the responses of well-established cells to ZC21 alloys and the effects of these established cells on alloy degradation in vitro. Both direct culture and direct exposure culture methods resemble in vivo conditions closely with the presence of physiologically relevant ions, proteins, and cells.[40] Furthermore, ZC21, ZSr41, and Mg pins were cultured with Gram-positive methicillin-resistant *Staphylococcus aureus* (MRSA) to determine their antibacterial activities. Finally, a mouse femoral defect model was used to study in vivo

degradation of ZC21 pins and associated biological responses for bone regeneration in comparison with ZSr41 and Mg pins for the first time. This comparison study focuses on in vitro versus in vivo evaluation of ZC21 alloy pins for orthopedic applications and bridges the critical knowledge gap on ZC21 alloys toward clinical translation in the future.

To highlight the significance of this study, recent development of Mg–Zn–Ca ternary alloys (since 2014) has been summarized in Table 1,[41–50] and the history of Mg–Zn–Ca alloys for biomedical applications before 2014 has been reported in our previous publication.[28] As shown in Table 1, different aspects of Mg–Zn–Ca alloys have been studied in recent years; for example, some work focused on the degradation behaviors of Mg–Zn–Ca alloys in vitro,[41,42,44,46–49] while others focused on the biocompatibility of Mg–Zn–Ca alloys.[43,45,50] To our knowledge, this is the first comparison study on characterization, mechanical properties, degradation behaviors, antibacterial properties, and biocompatibility of a promising Mg–Zn–Ca alloy in vitro and in vivo, which provides a comprehensive picture on the potential of Mg–Zn–Ca alloys for clinical translation when compared with pure Mg and the previously studied Mg–Zn–Sr alloy.[3,8,12,51–53]

2. MATERIALS AND METHODS

2.1. Preparation of ZC21 Pins and Controls.

ZC21 alloy in this study had a nominal composition of 2.0 wt % Zn and 0.5 wt % Ca in the Mg matrix. The alloy was produced by a metallurgical process consisting of melting, casting, extrusion and drawing. Briefly, a stainless steel crucible was first preheated in an electrical-resistance furnace (Shenyang General Furnace Manufacturing Co., Ltd.) to 400–500 °C, with 1.515 MPa argon (Ar) gas flowing into the furnace at a flow rate of 5 L/min to remove air. Pure Mg ingots (99.94 wt %; Boyu, Shenyang, China) were melted at a temperature of 700–730 °C in the stainless steel crucible under an Ar gas-protected environment to avoid oxidation, followed by removal of the surface scum. Commercially available bulk metallic Zn (99.5%; Boyu, Shenyang, China) and Mg-15Ca (wt %) intermediate alloy (Boyu, Shenyang, China) were added to the molten Mg, stirred, and heated at 750 °C for 20 min with Ar protection. After degassing with hexachloroethane and deslaging to ensure purity of the alloy, the molten mixture was cast at 720 °C in a cone-shaped cast iron mold and cooled down in the air. The cone-shaped mold had a bottom diameter of 50 mm, a top diameter of 70 mm, a height of 135 mm, and a wall thickness of 10 mm. The as-cast ingots were machined to rods with a diameter of 40 mm and a length of 100 mm for extrusion, and homogenized at 450 °C for 6 h. The 40 mm rods were then hot extruded at 250 °C with an extrusion ratio of 10:1 using a four-column hydraulic press (300 tons; Shandong Machinery Factory) to produce ZC21 rods with a diameter of 4 mm. Finally, the 4 mm alloy rods were drawn into a wire of 1 mm in diameter at 20 °C through multiple passes, that is, 4 → 3.5 → 3.0 → 2.8 → 2.7 → 2.6 → 2.5 → 2.4 → 2.3 → 2.2 → 2.1 → 2.0 → 1.9 → 1.8 → 1.7 → 1.6 → 1.5 → 1.4 → 1.3 → 1.2 → 1.1 → 1.0 mm, using a continuous wire drawing machine. Heat treatment was performed for the work piece at 300 °C for 30 min between each drawing pass.

Pure Mg wires were prepared using the same Mg source of the same purity of 99.94% and the same processing parameters of melting, casting, extrusion, and drawing as for producing

ZC21 alloy wires, to serve as a pure Mg control in this study. ZSr41 alloy, that is, Mg–4 wt % Zn–1 wt % strontium (Sr) alloy, was prepared using the same method as described in the previous publication,[12] and was included for comparison because it has been studied both in vitro and in vivo previously.[3,8,12,51–54] As-drawn titanium (Ti)-6 wt % aluminum (Al)-4 wt % vanadium(V) alloy wires with the same diameter of 1 mm (Baoti Group Ltd., Baoji, Shaanxi, China) were used as a nondegradable control in the in vitro studies with BMSCs and MRSA because Ti alloys represent the nondegradable metals that are currently used in major medical implants, such as bone fixation devices. We refer to this Ti alloy as T64. The 1 mm diameter wires of ZC21, Mg, and T64 were cut into 15 mm long pins for characterization and in vitro studies. Nonculture-treated glass disks (Fisher Scientific, 0.13–0.17 mm thick, Catalog No. 12–545–80) were used as a reference for in vitro culture with BMSCs and MRSA because it is a widely accepted standard for cell culture. For in vitro bacterial culture, ZC21, ZSr41, Mg and T64 were cut into 5mm long pins and nonculture-treated glass disks were used as reference. For in vivo study, the wires of ZC21, ZSr41, and Mg were cut into 2 mm long pins to fit into the femoral defect created in the animal model.

Before in vitro cell culture, in vitro bacterial culture, and in vivo implantation, the ZC21, ZSr41, Mg, and T64 pins were ground and polished using SiC paper (Ted Pella, USA) of 600, 800, and 1200 grit sequentially, and cleaned in 100% ethanol (200 proof; Koptec) with sonication (Symphony, VWR) for 5 min in between. Afterward, all samples were degreased in acetone (Sigma-Aldrich, USA) for 15 min, cleaned in 100% ethanol for 15 min with sonication, and dried in air at room temperature.

2.2. Surface Characterization of ZC21 Pins and Controls.

The surface appearance of ZC21, Mg, and T64 pins before and after polishing was examined using optical microscopy (SE303R-P, Amscope). The microstructure of ZC21, Mg, T64 pins and glass references after polishing was also characterized using scanning electron microscopy (SEM; Nova NanoSEM 450, FEI Co.) under the high vacuum mode. Surface elemental composition and distribution were analyzed using energy dispersive X-ray spectroscopy (EDS; Aztec, Oxford instruments, Abingdon, UK). An accelerating voltage of 15 kV was used to capture SEM images and perform EDS analyses. Glass references were sputter coated with Pt/Pd using a supper coater (Model 108, Cressington Scientific Instruments Ltd., Watford, UK) at 20 mA for 40 s of sputter time. To measure the grain size, ZC21 and Mg pins were mounted into epoxy (PACE Technologies, AZ, USA) and the surface along the length of pin was exposed for polishing. The samples were first ground with SiC papers up to 1200 grit, and fine polished using polycrystalline diamond paste (Physical Test Solutions, Culver City, CA, USA) from 6 to 0.25 μm. The etching solution was prepared by adding 10 mL of acetic acid (Sigma-Aldrich, USA), 4.2 g of picric acid (Sigma-Aldrich, USA), and 10 mL of distilled water into 70 mL of ethanol. The mounted Mg pins were dipped into the etching solution for about 2–8 s, while ZC21 pins were dipped for 15–20s until plenty of bubbles were observed. After etching, the samples were cleaned with ethanol, dried in air quickly at room temperature, and examined using a 3D laser microscope (VK-X150, Keyence, USA). Additionally, X-ray diffraction (XRD; Empyrean, PANalytical, Westborough, MA, USA) was used to analyze the crystal structures and phases present in ZC21 alloy and Mg pins. All XRD spectra were acquired using Cu Kα radiation

(45 kV, 40 mA) at a step size of 0.006° and a dwelling time of 50 s using a PIXcel 1D detector (PANalytical). Phase identification was performed using HighScore software (PANalytical).

2.3. Mechanical Testing of ZC21 Pins and Controls.

The compressive strength of ZC21 pins and Mg pins with a cylindrical geometry and a size of 1 mm in diameter and 2 mm in length was measured using a mechanical testing system (5969, Instron, Norwood, MA). The samples were photographed before and after compression testing. Specifically, for compression testing, a strain rate of 1 mm/min was applied on the samples. The stress–strain curves for each sample were plotted to determine the compressive modulus and ultimate compressive strength for each sample accordingly. After compression testing, the fracture surfaces of ZC21 and Mg were examined using SEM.

2.4. Corrosion Testing of ZC21 Pins and Controls Using Electrochemical Methods.

The corrosion properties of ZC21 pins and the control pins of ZSr41 and Mg were tested in a revised stimulated body fluids (rSBF) at 37 °C, using the electrochemical method established previously.[12,51] The cylindrical ZC21, ZSr41, and Mg pins had a dimension of 1 mm in diameter and 15 mm in length, and 2 mm of each pin was immersed in rSBF during testing. Potentiodynamic polarization (PDP) curves were recorded at a voltage scan from −0.5 to −3.0 V with a scanning rate of 10 mV/s using a potentiostat/galvanostat (Model 273A, Princeton Applied Research). The corrosion current I_{corr} and the corrosion potential E_{corr} were calculated by extrapolating the tangent line of the anodic and cathodic half of the curves according to the Tafel method in ASTM G102–89 standard. The corrosion current density J_{corr} was calculated by normalizing I_{corr} with the exposed surface area of each sample.

2.5. In Vitro Degradation and Cytocompatibility of ZC21 Pins and Controls in the BMSC/DMEM Culture System.

2.5.1. Preparation of BMSC Culture.—Following the protocol approved by the Institutional Animal Care and Use Committee (IACUC) at the University of California at Riverside (UCR), rat BMSCs were harvested and cultured according to the previously published procedures.[28,55] Briefly, the distal and proximal ends of the femoral and tibial bones were dissected, and the bone marrow was flushed out of the bone cavity and collected using DMEM (Sigma-Aldrich, St Louis, MO, USA) supplemented with 10% fetal bovine serum (FBS; HyClone, Logan, UT, USA) and 1% penicillin/streptomycin (P/S; Invitrogen, Grand Island, NY, USA). Hereafter, DMEM + 10%FBS + 1% P/S is referred to as DMEM. The collected cells were then filtered through a 70-μm nylon strainer (Fisher Scientific, NH, USA) to remove cell aggregates and tissue debris. The filtered BMSCs were cultured in DMEM under standard cell culture conditions (i.e., 37 °C, 5%/95% CO_2/air, humidified, sterile environment) to 90–95% confluency. Subsequently, BMSCs were detached using Trypsin (Fisher Scientific) and cultured up to the second passage (P2) for the in vitro cell studies with ZC21 pins and controls.

2.5.2. BMSC Culture with ZC21 Pins and Controls.—The cleaned and dried ZC21, Mg and T64 samples were first weighed individually and then disinfected under ultraviolet

(UV) radiation for 4 h before they were used in the cell studies. The glass references were disinfected under UV radiation for 2 h on each side. The wells of standard 12-well tissue culture treated plates were rinsed with 2 mL of PBS and 2 mL of DMEM to calibrate the osmotic pressure under sterile conditions. For the direct exposure culture method, BMSCs (P2) were first seeded into each well at a density of 20 000 cells/cm^2 and incubated in 3 mL of DMEM under standard cell culture conditions for 24 h. The disinfected samples were then placed directly on top of the cell layer without changing media and cultured for another 24 h. For the direct culture method, the samples and references were first placed in the culture wells, and BMSCs (P2) were then seeded directly onto the surfaces of the samples at a density of 20 000 cells/cm^2 and incubated in 3 mL of DMEM under standard cell culture conditions for 24 h. A positive control, designated as the “cells” group, consisted of BMSCs cultured with only DMEM in the wells, that is, without any samples. DMEM alone without cells and samples was also included as a blank reference and designated as the “‘media’” group. All samples and references were run in triplicate.

2.5.3. Surface Characterization of ZC21 Pins and Controls after in Vitro Cell Culture.—After the BMSC culture, the surfaces of ZC21, Mg, and T64 pins were examined again using optical microscopy. The surface microstructure and elemental composition of ZC21, Mg, T64, and glass were further characterized using SEM and EDS at an accelerating voltage of 15 kV under high vacuum mode. All samples were sputter coated with Pt/Pd at 20 mA for 40 s of sputter time before SEM imaging. XRD was used to determine the phases present in ZC21 alloy and Mg control after direct exposure culture and direct culture. The chemical bonding of the degradation products on the surfaces of ZC21 alloy and Mg control after culture was determined using Fourier transform infrared spectroscopy (FTIR, Thermo Fisher Scientific Nicolet iS10).

2.5.4. Characterization of BMSC Adhesion and Morphology.—After the prescribed cell culture, BMSCs attached on the samples and plates were fixed with 4% formaldehyde (10% neutral buffered formalin; VWR, Radnor, PA, USA) for 20 min. The fixed BMSCs were stained with Alexa Flour 488-phalloidin (A12379, Life technologies) for F-actin for 20 min and 4′,6-diamidino-2-phenylindole dilactate (DAPI, Invitrogen) for nuclei for 5 min. BMSCs attached on each sample (i.e., direct contact) and on the plate around each sample (i.e., indirect contact) were imaged using a fluorescence microscope (Eclipse Ti and NIS software, Nikon, Melville, NY, USA). DAPI-stained nuclei were counted to determine cell adhesion density per unit area. At least five fluorescence images of BMSCs under direct contact conditions and nine fluorescence images of BMSCs under indirect contact conditions were used for cell counting and statistical analyses of the data.

2.5.5. In Vitro Degradation of ZC21 Pins in the BMSC Culture.—After the prescribed cell culture, each sample was dried and weighed again. The initial and final mass of each sample were used to calculate the mass ratio, that is, final/initial mass. The pH of the postculture media was measured using a precalibrated pH meter (Symphony, Model SB70P, VWR) immediately after collection of the media. The concentrations of Mg^{2+}, Zn^{2+}, and Ca^{2+} ions in the postculture media were measured using inductive coupled plasma–optical emission spectrometry (ICP-OES, Optima 8000, PerkinElmer). Before ICP-OES, the media

of all groups were diluted in deionized (DI) water to minimize the matrix effects. For the measurements of Mg^{2+} and Ca^{2+} ions, the media were diluted in deionized water at a ratio of 1:100. For the measurement of Zn^{2+} ion, the media were diluted in deionized water at a ratio of 1:10. The ICP-OES was calibrated using Mg^{2+}, Zn^{2+}, and Ca^{2+} standard solutions that were diluted to the ranges of 0.5–5.0, 0.1–1.0, and 0.1–1.0 mg/L, respectively.

The degradation rates of ZC21 pins and Mg control pins were calculated as the daily release rate of Mg^{2+} ions into the culture media. According to the equation of the degradation reaction (eq 1), Mg^{2+} ion release is a direct indicator of the degradation process.

$$\mathrm{Mg(s) + 2H_2O(1) \rightarrow Mg^{2+} + 2OH^- + H_2(g)} \quad (1)$$

The daily degradation rates of ZC21 and Mg into culture media were calculated following eq 2.

$$R = \frac{(C_{\mathrm{Mg}} - C_0) \times V}{A \times t} \quad (2)$$

In eq 2, R represents the daily degradation rates, C_{Mg} represents the Mg^{2+} ion concentration in the media measured after 24-h culture with a sample, C_0 represents the mean Mg^{2+} ion concentration in the DMEM blank reference measured after 24-h culture, V represents the volume of culture media in each culture well (i.e., 3 mL), A represents the surface area of the sample, and t represents the culture time, that is, $t = 1$ day for the 24-h period. C_0 is the baseline of Mg^{2+} ion concentration in the DMEM media for each group, and thus, it should be subtracted from the measured total Mg^{2+} ion concentration in the postculture media to obtain the actual concentration of Mg^{2+} ions released from degradation of Mg-based samples. The daily release rates of Mg^{2+} ions into the culture media could be used for direct comparison of the degradation rates of different sample groups, for example, ZC21 pins and Mg controls. The width and area of corrosion cracks on the surfaces of ZC21 and Mg after direct exposure culture and direct culture were determined based on their corresponding SEM images, using quantitative image analysis tools in ImageJ. The crack width was defined as the gap distance between the two edges of the crack. The crack area ratio was defined as the ratio of crack area over the whole SEM image area. Specifically, the “straight line” tool was used to draw lines for determining crack width, while the “freehand selections” tool was used to outline the crack area and to determine the crack area ratio. The crack width and crack area ratio were measured in three images for each group, and five measurements were performed in each SEM image for statistical analyses of the data.

2.6. Bacterial Culture with ZC21 Alloy, ZSr41 Alloy, and Mg Pins in Vitro.

2.6.1. Preparation of Bacterial Culture.—The frozen stock of methicillin-resistant *Staphylococcus aureus* (MRSA) was stored at −80 °C. A sterile loop was used to transfer a portion of the frozen stock to the tryptic soy broth (TSB; Fluka Analytical, Sigma-Aldrich). The frozen MRSA was retrieved and cultured in tryptic soy broth (TSB; Fluka Analytical, Sigma-Aldrich) overnight using a shaker incubator (Incu-shaker Mini, Benchmark Scientific) at 37 °C and 250 rpm for 16 h. A 10 μL of the bacteria stock was added into 5 mL of fresh TSB and incubated for another 4–6 h at 37 °C and 250 rpm. The as-grown bacteria

was then washed 3 times with revised simulated body fluid (rSBF) to remove any residual TSB and resuspended in rSBF supplemented with 10% FBS. The concentrations of MRSA were first determined using a hemocytometer (Hausser Bright-Line 3200, Hausser Scientific), and then, the MRSA suspension was diluted to a concentration of 7.5×10^5 cells/mL in rSBF supplemented with 10% fetal bovine serum (FBS). The MRSA concentration of 7.5×10^5 cells/mL was used to match the reported concentration that causes orthopedic infections clinically.[55] After dilution to 7.5×10^5 cells/mL, 0.75 mL of MRSA suspension was added to each well of a 48-well nontissue culture treated polystyrene plate (Corning, Falcon 351143) that contained the samples and controls and incubated for 24 h in the shaker incubator at 37 °C and 120 rpm. The initial seeding density was confirmed by plating the diluted MRSA stock onto the agar plates and counting the colony forming units (CFUs).

2.6.2. Characterization of MRSA Concentration, Adhesion, and Morphology.

—After 24-h bacterial culture, the postculture broth was collected and the MRSA concentration in the collected broth was measured by counting the colony forming units (CFU) plated on the agar plates. For this purpose, each collected postculture suspension was diluted using a suitable dilution factor that can lead to a reasonably countable number of CFUs. For agar plating, a 100 μL of diluted suspension was individually pipetted onto the agar plate, and evenly spread using a glass spreader. The agar plates were then inverted and incubated for 16–18 h.

To determine the density of bacteria adhered on the samples, two samples from each group were placed individually in microcentrifuge tubes with 2 mL of rSBF. The microcentrifuge tubes were then sonicated in a sonication bath for 10 min, and at each 5 min, they were vortexed for 5 s. After that, the adhered bacteria were detached from the sample surfaces and collected in the rSBF. The MRSA concentration in the collected rSBF was measured by counting the colony forming units (CFU) plated on the agar plates following the same method of agar plating and CFU counting as described above.

To determine the adhesion and morphology of bacteria on the sample surfaces, one sample from each group was analyzed using SEM imaging. The bacteria on the surface were first fixed with 10% glutaraldehyde (Sigma-Aldrich) for 1 h and then rinsed 3 times with a Tris-buffered saline (Sigma-Aldrich). The samples were then dehydrated using 25%, 75% and 100% ethanol for 30 min each and dried in air at room temperature for 24 h. The dried samples were sputter-coated with Pt/Pd for 60 s at 20 mA, prior to the SEM imaging.

2.6.3. In Vitro Degradation of ZC21 Pins in the MRSA Culture.—

The pH of the postculture rSBF with 10% FBS was measured using a precalibrated pH meter (Symphony SB70P, VWR). The postculture rSBF with 10% FBS was then diluted with DI water to 1:100 to analyze the Mg^{2+} and Ca^{2+} ion concentrations, and diluted with DI water to 1:10 to analyze the Sr^{2+} ion concentration in the media cultured with ZSr41 using ICP-OES similarly as described above in 2.5.5. All the groups were run in triplicates. Finally, the degradation rates of ZC21 pins, ZSr41 pins, and Mg control pins were calculated as described above in section 2.5.5.

2.7. In Vivo Degradation of ZC21 Alloy, ZSr41 Alloy, and Mg Pins and Bone Regeneration in Mouse Femoral Defects.

2.7.1. Animal Model and Surgical Procedures.—Nine 10-week-old male mice were used in the present study and randomly assigned to three groups ($n = 3$ per group). The Institutional Animal Care & Use Committee (IACUC) at the University of Southern California approved the experimental protocol (#9320). Before initiation of anesthesia for each animal, buprenorphine (0.5 mg/kg of animal weight; Buprenorphine SR-LAB 1 mg/mL; ZooPharm, Windsor, CO, USA) was administered subcutaneously as a sedative and preventive analgesic. The analgesic effect of this medication lasts at least 72 h throughout surgery and postoperative recovery. Anesthesia was induced and maintained using ~2% isoflurane (Fluriso, NDC 13985–046, VETone, ID, USA) and 0.3 L/min of oxygen flow.

Anesthetized mice were positioned on the operating table in a prone position with the left leg facing downward. The operation site was aseptically prepared. A posterior-lateral approach was used to expose the lateral surface of the femur by separating the muscles. The periosteum of the femur was incised, and then the femur was exposed using a retractor. Following predrilling using a drill with a diameter of 0.31 mm on the posterior lateral side of the exposed femur, four stainless steel screws were used to stabilize the 6-hole plastic plate (RISystem AG, Davos, Switzerland) with a drill and saw guide (jig). Two Gigli saws (0.22 mm; RISystem) were then inserted, one in each of the two slots in the jig, and a 2 mm long mid-diaphyseal femoral ostectomy was subsequently performed. The jig was then removed and the two end screws locked the plate in place. The surgical field was copiously lavaged with sterile isotonic saline. The defect was filled with the filling materials of interest, that is, pins of ZC21 alloy, ZSr41 alloy, and pure Mg control. Sham designates the reference group with femoral defect only, that is, no pin implant. In all animals, the fascia and subcutaneous planes were closed with a simple continuous suture pattern using 5–0 Vicryl rapid sutures. Skin closure was accomplished using a simple interrupted suture pattern using 4–0 Prolene.

2.7.2. Monitoring the Healing of Femoral Defects and the Degradation of Pins.—X-ray radiography (In-vivo Xtreme X-ray; Bruker) was used to monitor the degradation of pin implants and healing of femoral defects in situ at 4, 8, and 12 weeks after surgery. The size of the gap created between the two cut ends of the femur was measured on the radiographs at each time point using ImageJ.

2.7.3. Characterization of the Pin Implants after 12 Weeks of Implantation.—After 12 weeks of implantation in the femurs of mice, all tissues and samples were fixed and stored in 4% paraformaldehyde (PFA). The surfaces of ZC21, ZSr41, and Mg pins were examined using optical microscopy before and after 12 weeks of in vivo implantation. Mg pins degraded completely after 12 weeks. All samples were weighed before and after 12 weeks of implantation. The initial and final masses of each sample were used to calculate the mass ratio, that is, final/initial mass.

The daily degradation rates of ZC21 and ZSr41 were calculated using eq 3.

$$R = \frac{(M - M_0)}{A \times t} \quad (3)$$

In eq 3, R represents the daily degradation rate, M represents the mass of a sample after 12 weeks of implantation, M_0 represents the mass of a sample before implantation, A represents the surface area of a sample, and t represents the implantation time, that is, $t = 84$ days for the 12-week period. SEM images were taken on the surface region of ZC21 and ZSr41 after the loose deposition layer was removed to identify crack width and area using ImageJ.

Surface topography and elemental composition of the surfaces of ZC21 and ZSr41 pins after implantation for 12 weeks were characterized using SEM and EDS, respectively. Additionally, elemental distribution maps on the surfaces of dissected pins were obtained for Mg, carbon (C), oxygen (O), phosphorus (P), Ca, sodium (Na), and potassium (K) (Kα lines). XRD was used to determine the phases present on the surfaces of ZC21 and ZSr41 pins. The chemical bonding of the degradation products on the surfaces of ZC21 and ZSr41 pins were examined using FTIR. Experimental settings for SEM, EDS, XRD, and FTIR were the same as described above in sections 2.2 and 2.5.3.

2.8. Statistical Analyses.

All numerical data used in this study were obtained from experiments run in triplicate. The numerical data on the adhesion density of BMSCs under direct contact and under indirect contact conditions, sample mass ratio, pH in the culture media, ion concentrations in the culture media, daily release rates of Mg^{2+} ions, and width and area of corrosion cracks on the surfaces of ZC21 and Mg pins were examined using two-way analysis of variance (ANOVA), followed by posthoc test. The statistical analysis was performed using GraphPad Prism 7 software. Statistically significant differences were considered at $p < 0.05$.

3. RESULTS

3.1. Microstructure, Elemental Composition, Mechanical Properties, and Corrosion Properties of ZC21 Pins and Controls.

Figure 1a and b are the optical images of metallographic samples of ZC21 and Mg pins. Clearly, the microstructures in Figure 1a and b confirmed that the grain size of ZC21 was much smaller than that of Mg, that is, the addition of Zn and Ca into Mg substrate could refine the grain size. Figure 1c–g shows the SEM images and surface elemental compositions (wt %) of ZC21 alloy pin, Mg pin, T64 pin, and glass reference. In Figure 1c, at low magnification (500×), ZC21 and Mg showed random white precipitates on the surface that could be traces of oxides or hydroxides, and T64 showed typical alloy microstructure with secondary phase on the surface. Polishing traces were barely visible in the low-magnification SEM images. However, at high magnification (5000×), polishing traces were visible on the surfaces of ZC21, Mg, and T64 samples. The surface of the glass reference appeared smooth without any visible features at both low and high magnification. Figure 1d shows the elemental composition on the surface of ZC21 acquired by EDS area and point analyses. The EDS analysis of the whole image area of ZC21 at low magnification (500×) showed 95.6 wt % Mg, 2.0 wt % Zn, and 0.4 wt % Ca, which confirmed the nominal

composition of ZC21 alloy. The EDS point analyses at high magnification (5000×) showed consistent results, that is, similar to the EDS area analysis on ZC21 alloy. Specifically, for ZC21, point 1 showed 94.5 wt % Mg, 1.8 wt % Zn, and 0.4 wt % Ca, while point 2 showed 96.0 wt % Mg, 2.0 wt % Zn, and 0.3 wt % Ca. Figure 1e shows the EDS area and point analyses of Mg. Specifically, the EDS results of Mg at 500× and at points 3 and 4 at 5000× showed 94.3 wt % Mg, 94.6 wt % Mg, and 93.2 wt % Mg, respectively; small amounts of carbon (C) and oxygen (O) were also detected. In Figure 1f, the EDS results of T64 at 500× and at points 5 and 6 at 5000× all showed similar elemental composition. Specifically, T64 area analysis showed 88.6 wt % titanium (Ti), 5.5 wt % aluminum (Al), and 3.4 wt % vanadium (V); point 5 showed 88.6 wt % Ti, 6.0 wt % Al, and 2.5 wt % V, and point 6 showed 88.8 wt % Ti, 6.0 wt % Al, and 3.4 wt % V. As for glass reference, 41.1 wt % silicon (Si), 15.1 wt % sodium/potassium (Na/K), 1.6 wt % carbon (C), and 42.3 wt % oxygen (O) were detected in EDS area analysis at low magnification, as shown in Figure 1g.

The mechanical properties of Mg–Zn–Ca alloys have been reported previously,[33,35,39,56] and the results showed that Mg–Zn–Ca alloys exhibited higher Young's modulus and higher tensile strength than pure Mg. Specifically, as-cast Mg had a Young's modulus of 41 GPa and a tensile strength of 86.8 MPa.[39,56] As-cast Mg-4Zn-0.5Ca alloy showed a tensile strength of 180 MPa,[33] while the extruded Mg–4.0Zn–0.2Ca alloy exhibited a tensile strength of 297 MPa and Young's modulus of 45 GPa.[35] On the basis of these previous reports, ZC21 is expected to have higher mechanical strength than pure Mg. However, different processing parameters and testing conditions could affect the results, even when the alloy composition is the same or similar. Thus, the ZC21 pins that had the same processing parameters and sample dimension as the in vivo implants in mice were still mechanically tested to confirm. Both tensile and compressive properties are important for clinical applications, but we performed the compression test to mimic the condition of in vivo implantation in mouse femoral model in this study. The results of compression testing for ZC21 and Mg pins are shown in Figure 2. The samples were compressed to the point where they became fractured, as shown in Figure 2a and b. The representative stress–strain curves for ZC21 and Mg pins are plotted in Figure 2c. The ultimate compressive strength in Figure 2d and the compressive modulus in Figure 2e were determined based on all the stress–strain curves. ZC21 showed a statistically higher compressive strength and compressive modulus than Mg because of the addition of Zn and Ca as alloying elements. Specifically, the compressive strengths of ZC21 and Mg were 321.1 ± 13.6 and 262.7 ± 8.3 MPa, respectively. The compressive modulus of ZC21 and Mg were 4.13 ± 0.15 and 3.10 ± 0.10 GPa, respectively. Not surprisingly, the deformation of ZC21 and Mg pins under mechanical stress was observed in Figure 2f–g. The microcracks on the surface of fractured ZC21 sample appeared smaller than that of Mg.

Figure 3a shows the representative potentiodynamic polarization (PDP) curves of ZC21 pins and the control pins of ZSr41 and pure Mg. Figure 3b shows the corrosion potential (E_{corr}) and corrosion current density (J_{corr}) of ZC21 pins and the control pins of ZSr41 and pure Mg, which were extrapolated based on the Tafel method. ZC21 and Mg exhibited a statistically significant more negative E_{corr} than ZSr41. Mg showed statistically significant higher J_{corr} than ZC21 and ZSr41. Overall, the results indicated that Mg had the least corrosion resistance when compared with the ZC21 and ZSr41 alloys.

3.2. BMSC Responses and Degradation of ZC21 Pins and Controls in Vitro.

3.2.1. Surface Analysis before and after in Vitro BMSC Culture.—Figure 4 shows optical micrographs of ZC21, Mg, and T64 pins before polishing, after polishing, after 24-h direct exposure culture, and after 24-h direct culture. Before polishing, the surfaces of all metallic samples showed nonhomogeneous oxidation with dark coloration. After polishing, the oxide layers were removed and the surface became shiny. After direct exposure culture and direct culture, white precipitates appeared on the surfaces of ZC21 and Mg, while the surface of T64 showed no visible change.

Figure 5 shows the SEM images and surface elemental compositions (wt %) of ZC21, Mg, T64, and glass after 24-h direct exposure culture and 24-h direct culture. In Figure 5a, more white precipitates were observed on ZC21 at the low magnification of 500× than on Mg after both culture methods. At the high magnification of 5000×, localized corrosion and cracks became more visible on the surfaces of ZC21 and Mg when compared with the respective low-magnification SEM images. After direct culture, cracks on the ZC21 surface were slightly smaller than on the sample cultured using the direct exposure method. As for Mg, localized corrosion was more severe and cracks on the surface were significantly larger than on ZC21 in both culture methods. T64 showed the same surface morphology as before culture at the low magnification of 500× for both culture methods; at high magnification of the 5000×, some deposition on the T64 surface became visible, possibly from the cell culture. On the glass reference, salt deposition appeared on the surface after both culture methods. Figure 5b shows the surface elemental composition of all samples at low magnification of 500× after 24-h direct exposure culture. ZC21 showed a significant decrease in Mg (35.2 wt %) and Zn (1.3 wt %) content because of the degradation layers formed on the surface. However, more Ca (1.3 wt %) was detected on ZC21, which indicated that the degradation layers contain Ca deposited from the culture. Both C (18.9 wt %) and O (36.2 wt %) increased significantly, and new salt elements, including phosphorus (P), Na, K and chlorine (Cl), were also detected. The Mg sample showed a decrease of Mg (30.2 wt %) and an increase of C (21.1 wt %) and O (35.9 wt %). Ca (1.0 wt %), P (9.2 wt %), and Na/K/Cl (2.5 wt %) were new salt elements detected on the surface of Mg. As for T64, not surprisingly, less Ti (74.4 wt %), Al (4.3 wt %), and V (3.3 wt %) but more C (7.3 wt %) and O (10.7 wt %) were detected. Glass had 9.9 wt % Na/K/Cl after culture. When comparing the EDS results after direct exposure culture (Figure 5b) versus direct culture (Figure 5c), each sample showed a similar increasing or decreasing trend to the EDS results before culture; however, the exact elemental compositions of each sample differed under the two different culture methods. For example, more Ca deposition onto ZC21 and Mg was found under direct culture method than the DE method.

Figure 6 shows XRD and FTIR spectra of ZC21 and Mg before and after cell culture. Specifically, in Figure 6a, XRD spectra of ZC21 before culture, after 24-h direct exposure culture, and after 24-h direct culture showed the presence of different phases before and after culture. The relevant phases were identified based on Mg (ICSD pattern 01–089-7195), MgO (ICSD pattern 01–070-9183), $Mg_{0.97}Zn_{0.03}$ (ICSD pattern 01–071-9628), Ca_5Zn_3(ICSD pattern 01–073-8016), $Ca(OH)_2$ (ICSD pattern 01–073-8394), and $CaCO_3$ (ICSD pattern 01–085-1108). The XRD pattern of ZC21 before culture indicated an α-Mg

phase accompanied by $Mg_{0.97}Zn_{0.03}$and Ca_5Zn_3 phases. After direct exposure culture, MgO and $Ca(OH)_2$ phases were detected. After direct culture, MgO, $Ca(OH)_2$, and $CaCO_3$ phases were detected. Figure 6b shows XRD spectra of Mg before culture, after 24-h direct exposure culture and after 24-h direct culture. The relevant phases were identified based on Mg (ICSD pattern 01–089-7195), MgO (ICSD pattern 01–070-9183) and $Mg(OH)_2$ (ICSD pattern 01–078-3960). After both culture methods, MgO and $Mg(OH)_2$ were detected on the Mg control samples. In the FTIR spectra, O–H and CO_3^{2-} functional groups were identified for ZC21 and Mg control samples after both culture methods, as shown in Figure 6c and 6d, respectively.

3.2.2. Cell Morphology and Adhesion after Culture with ZC21 Pins and Controls.—

Figure 7 shows the representative fluorescence images of BMSCs adhered on the sample surface (direct contact) and on the culture plates surrounding the respective samples (indirect contact) after 24-h direct exposure culture and 24-h direct culture. Under the direct contact conditions in the direct exposure culture, ZC21 had more cells attached to the surface than T64 or glass, but the surface of Mg had no cells attached. Under the direct contact conditions in the direct culture, BMSCs attached to the ZC21 surface but no cells attached to the Mg surface. T64 and glass had more cells attached on their surfaces under direct contact conditions in the direct culture than did their counterparts in the direct exposure culture. Under the indirect contact conditions, the ZC21, Mg and T64 groups showed greater cell adhesion than under the direct contact conditions in the same culture methods. All groups showed more BMSCs attached on the plate surrounding each sample in direct exposure culture than in direct culture, most likely because the BMSCs in the direct exposure culture were precultured for 24 h.

BMSC adhesion density was quantified based on the fluorescence images after 24-h direct exposure culture and 24-h direct culture, as shown in Figure 8. In direct exposure culture in Figure 8a, ZC21 showed statistically higher cell density in direct contact conditions than Mg, T64, and glass. In direct culture, ZC21, Mg, and T64 showed statistically lower cell density under direct contact conditions than glass. Under direct contact conditions, the cell density on ZC21 samples was statistically greater than on Mg controls in both culture methods. The Mg control group showed a statistically lower cell density than T64 and glass under direct contact conditions in both culture methods. Figure 8b shows the quantified cell density under indirect contact conditions in each group, and importantly, ZC21 showed statistically higher cell density than Mg controls, but no statistical difference in cell density when compared with T64 and cell-only groups in both cell culture methods.

3.2.3. In Vitro Degradation of ZC21 and Mg Pins in the BMSC/DMEM Culture Systems.—

Changes in sample mass, pH of postculture media, and ion concentrations in the postculture media are the key indicators of degradation of Mg-based samples. Figure 9 shows the mass ratio of the samples (that is, final mass/initial mass) and pH values of the media collected from each well after 24-h direct exposure culture and 24-h direct culture. As expected, in both culture methods in Figure 9a, the mass change of all samples was small because of the short culture period. No statistically significant difference was found among the mass changes of all samples. As shown in Figure 9b, the pH values ranged from 8.3 to

8.4 among all the groups in direct exposure culture, and no statistically significant differences were found. In direct culture, pH values ranged from 7.9 to 8 and the pH differences across the groups were small, even though statistically significant differences were found.

Figure 10a–c shows the Mg^{2+}, Zn^{2+}, and Ca^{2+} ion concentrations in the media collected from each well after 24-h direct exposure culture and 24-h direct culture. In Figure 10a, in both culture methods, ZC21 and Mg control pins showed statistically higher Mg^{2+} ion concentrations than T64, glass, cell-only and media groups. After 24-h direct exposure culture, ZC21 showed the highest Mg^{2+} ion concentration, but no statistically significant difference was found between ZC21 and the Mg control group. Interestingly, after 24-h direct culture, Mg showed the highest Mg^{2+} ion concentration, but again no statistical difference between ZC21 and Mg was detected. In Figure 10b, as expected, the ZC21 group showed the highest Zn^{2+} ion concentration, which was statistically higher than all the other groups in both culture methods. In Figure 10c, after 24-h direct exposure culture, ZC21 showed the lowest Ca^{2+} ion concentration in the postculture media and statistically significant difference was found between ZC21 and the cell-only control group. Interestingly, after 24-h direct culture, ZC21 showed the highest Ca^{2+} ion concentration, which was statistically higher than that of the T64, glass and media groups. Figure 10d shows the daily degradation rates of ZC21 and Mg, which were calculated based on the daily release rates of Mg^{2+} ions into the media after 24-h direct exposure culture and 24-h direct culture. In direct exposure culture, ZC21 showed a statistically higher degradation rate than Mg. In direct culture, Mg showed a higher average degradation rate than ZC21, but no statistically significant difference was found. Figure 10e–f shows the crack width and crack area ratios on the surfaces of ZC21 and Mg, as quantified based on SEM images after culture. In both culture methods, ZC21 showed statistically smaller crack width and crack area ratios than the Mg controls, indicating that ZC21 provided a more desirable degradation mode than Mg for medical applications.

3.3. Antibacterial Property of ZC21, ZSr41, and Mg Pins in Vitro.

As shown in Figure 11a, after 24-h culture with MRSA, localized corrosion and cracks were observed on the surfaces of ZC21, ZSr41, and Mg in Figure 11a and appeared more clearly at the high original magnification of 5000×. Localized corrosion appeared more severe on the surface of ZSr41 when compared with that of ZC21 and Mg.

The viable MRSA in the culture suspension and on the sample surface was quantified as the colony forming units (CFUs), after 24-h culture with each sample group, as shown in Figure 11b. No inhibition of MRSA growth in the culture suspensions was found for all groups. However, the CFUs of MRSA on Mg-based and control samples were all significantly lower than the respective CFU of MRSA in suspensions for the same sample or control groups. Generally, MRSA bacteria seem to grow in suspensions more than adhere onto the substrates, including the standard substrates of glass reference, which is in agreement with our previous finding.[57] Interestingly, the CFU of MRSA on the surface of ZC21 was significantly lower than the other groups including the T64 and glass control groups,

indicating ZC21 surface had the strongest antibacterial activity against the adhesion and growth of MRSA.

As expected in Figure 12a, the pH values of postculture broths collected from the groups of ZC21, ZSr41, and Mg were significantly higher than the control groups of T64, glass, MRSA only, and broth only, because their degradation in rSBF with FBS released OH^- ions. The analysis of ionic concentrations in Figure 12b–c confirmed that Mg^{2+} ion concentrations in the groups of ZC21, ZSr41, and Mg were statistically higher than the control groups of T64, glass, and rSBF only. The average Ca^{2+} ion concentrations in the groups of ZC21, ZSr41, and Mg were lower than the control groups because Ca-containing minerals deposited on the surface but no statistically significant difference was found.

3.4. In Vivo Study of ZC21, ZSr41, and Mg Pins in Mouse Femoral Defects.

3.4.1. In Vivo Degradation of ZC21, ZSr41, and Mg Pins and Bone Healing in the Femoral Defects.—

During the postsurgery observation period, neither wound complication nor implant failure occurred. Stable bone fixation was maintained in all animals throughout the in vivo study. Figure 13 shows the representative X-ray radiographs of the mouse femoral bone defects at 4, 8, and 12 weeks after implantation of ZC21, ZSr41, and Mg pins. The radiographs in Figure 12 confirmed the gradual degradation of ZC21, ZSr41, and Mg pins in vivo, and indicated different degrees of bone regeneration in the femoral defects in response to different pin implants. Specifically, ZC21 pins (Figure 13a1–a3) and ZSr41 pins (Figure 13b1–b3) maintained their shape and structure with a slight volume reduction after 12 weeks of implantation. Mg pins (Figure 13c1–c3) had the fastest degradation among all of the Mg-based pins. After 8 weeks of implantation, Mg pins became nearly invisible in radiographs. The ZC21 group achieved the most promising healing results when compared with the other two Mg-based groups and the sham group. In the ZC21 group, the gaps between the bone ends reduced to 0.78 ± 0.37, 0.67 ± 0.32, and 0.57 ± 0.27mmat 4, 8, and 12 weeks after implantation, respectively. The gaps in the ZSr41 group were 1.26 ± 0.11, 1.15 ± 0.16, and 0.97 ± 0.22 mm at 4, 8, and 12 weeks after implantation, respectively. The gaps in the Mg group were 1.26 ± 0.21, 1.20 ± 0.18, and 1.15 ± 0.15 mm at 4, 8, and 12 weeks after implantation, respectively. The sham group with no implants showed the gap sizes of 1.29 ± 0.07, 1.19 ± 0.05, and 1.17 ± 0.06 mm at 4, 8, and 12 weeks after implantation, respectively. Clearly, the size of gap defect in the ZC21 group became the smallest at the prescribed time points when compared with the other groups, indicating that ZC21 pins had the highest osteogenic potential for bone healing and regeneration.

3.4.2. Surface Characterization of ZC21 and ZSr41 Pins after in Vivo Implantation.—

Figure 14 shows the surface morphology and degradation properties of ZC21, ZSr41, and Mg pins before and after 12 weeks of in vivo implantation in a mouse femoral defect. ZC21 retained its shape and showed a slight volume reduction. White degradation layers covered the surface of ZC21, as shown in Figure 14a. ZSr41 also developed white deposits on the surface, similar to ZC21, but ZSr41 had more volume reduction than ZC21. Mg completely degraded after 12 weeks. After 12 weeks of implantation, the average mass ratio (final/initial mass) was 0.32 for ZC21, 0.14 for ZSr41,

and 0 for Mg, as shown in Figure 14b. These ratios serve as an indicator of the in vivo degradation of ZC21, ZSr41, and Mg pins. Specifically, the daily degradation rates of ZC21, ZSr41, and Mg were calculated to be 0.28 ± 0.09, 0.37 ± 0.09, and 0.63 mg cm^{-2} d^{-1}, respectively (Figure 14c). The daily degradation rate of Mg was calculated based on the initial sample mass and 12-week degradation time, since Mg pins fully degraded by 12 weeks. The crack width and crack area on the surfaces of ZC21 and ZSr41 were identified on the SEM images of the pin samples in Figure 14d–e after implantation. The cracks on the exposed surfaces of ZC21 and ZSr41 are clearly visible in these figures. Figure 14f and 14g show the quantified crack width and crack area ratios for ZC21 and ZSr41, respectively. Specifically, ZC21 showed a mean crack width of 8.05 ± 0.23 μm, which was significantly greater than that of ZSr41. However, the average crack area ratio of ZC21 was slightly less than that of ZSr41, though there was no statistically significant difference.

The residual ZC21 and ZSr41 pins that were dissected out after 12 weeks of implantation in a mouse femur were characterized, as shown in Figure 15. Degradation products covered most of the surfaces of ZC21 and ZSr41 pins, as shown in Figure 15a1 and 15b1, respectively. The corresponding EDS elemental distribution maps in Figure 15a2–a8 and 15b2–b8 revealed the deposition of Ca and P in vivo and the presence of Mg, C, O, Na, and K on the surfaces of both ZC21 and ZSr41, which were confirmed by the surface elemental composition (wt %) quantified through EDS area analyses in Figure 15c. Specifically, the ZC21 pin had (wt %) 10.5% Mg, 13.0% C, 44.8% O, 18.2% P, 5.8% Ca, 7.7% Na/K on the surface; the ZSr41 pin showed (wt %) 9.6% Mg, 11.7% C, 45.4% O, 17.2% P, 9.0% Ca, 7.1% Na/K on the surface. XRD results in Figure 15d confirmed the presence of $Mg_3(PO_4)_2{\cdot}8H_2O$, $MgCO_3{\cdot}3H_2O$, and $CaCO_3$ phases on the surfaces of ZC21 and ZSr41 pins after 12 weeks of implantation. Additionally, in Figure 15e, O–H, C=C, and CO_3^{2-} functional groups were identified in the FTIR spectra of ZC21 and ZSr41 after in vivo implantation.

4. DISCUSSION

In this study, we investigated microstructure and mechanical and corrosion properties of Mg–Zn–Ca alloy; reported the degradation and cytocompatibility of Mg–Zn–Ca alloy in two different cell culture methods; studied the effects of soluble and insoluble degradation products on cell adhesion and viability in vitro; analyzed different degradation behaviors of Mg–Zn–Ca alloy in vitro and in vivo; compared the antibacterial effects of Mg–Zn–Ca alloy and degradation in bacterial culture with a previous Mg–Zn–Sr alloy; and determined the degradation rates of Mg alloys of interest in different in vitro culture systems (including both BMSC culture and MRSA bacterial culture) versus in vivo in an animal model.

4.1. Improved Cytocompatibility and Antibacterial Properties in Vitro and Enhanced Bone Regeneration in Vivo for ZC21 Pins.

Cytocompatibility of various as-cast Mg–Zn–Ca alloys with bone marrow derived mesenchymal stem cells (BMSCs) has been studied previously using the direct culture method in vitro.[28] It is still necessary to study the as-drawn ZC21 pins in BMSC culture, because the different processing conditions for as-cast Mg–Zn–Ca alloy plates versus as-drawn wires could lead to different cell responses, even when the alloy composition is the

same. In addition to the direct culture method, the direct exposure culture method was included in this study to mimic the *in vivo* interactions of the ZC21 pin implants with established BMSCs in the body. The ZC21 alloy was found to be cytocompatible with BMSCs under direct contact and indirect contact conditions in both of the culture methods in this study. The cells face different surface and local environment under the direct versus indirect contact conditions even in the same culture wells. Generally, the factors that affect BMSC adhesion and function on and around Mg-based materials include surface microstructure and composition as well as the presence of degradation products, both soluble and insoluble. Soluble degradation products include the ions such as Mg^{2+}, Zn^{2+}, Ca^{2+}, and OH^{-} ions that affect media pH and composition when they were released into the media. Insoluble degradation products include nondegradable compounds formed on the surface of Mg alloys during the degradation and precipitation processes, such as hydroxides, carbonates, and phosphates. Under the direct contact condition, surface microstructure and insoluble degradation products on the sample surface play key roles on cell adhesion, while the dynamic pH and ion concentrations at the sample surface affect cell adhesion and functions as well. In contrast, under indirect contact condition, soluble degradation products released into the media, that is, media pH and ion concentrations, are the key factors that influence cell adhesion and functions, because cells have no contact with sample surface. When the chemistry and microstructure at the sample surface are beneficial for cell growth, it is possible to have higher cell density in direct contact condition than indirect contact condition. For example, the cell density on ZC21 surface (direct contact) was higher than that on plate (indirect contact) in both culture methods; in contrast, the cell density on Mg surface was lower than that on plate in both culture methods. Because the ZC21 and Mg pins were polished following the same method before cell culture, we expected them to have similar surface roughness. Thus, this factor was not considered as primarily responsible for the differences observed in BMSC adhesion and spreading between the ZC21 and Mg groups in this study. Comprehensive characterization of their surface microstructure and composition suggested that the formation of Ca-containing minerals on the surface of ZC21 likely created a more favorable interface for the attachment and spreading of BMSCs under direct contact conditions. Specifically, after BMSC culture, more deposits appeared on the surface of ZC21 than on Mg (Figures 4 and 5a). On the basis of the EDS analyses (Figure 5), the Ca content on ZC21 was higher than on pure Mg after both direct exposure and direct cultures, indicating more Ca deposition on the surface of ZC21. The XRD spectra (Figure 6) confirmed the presence of $Ca(OH)_2$ phase on the surface of ZC21 after direct exposure culture and the presence of $Ca(OH)_2$ and $CaCO_3$ phases after direct culture, but no Ca-containing minerals were detected on the surface of Mg in either culture method. In direct exposure culture, Ca^{2+} ion concentration in the culture with ZC21 alloy was the lowest among all groups, suggesting that some Ca in the media might have been deposited into the degradation layer on the ZC21 surface. Interestingly, in direct culture, the ZC21 alloy showed the highest Ca^{2+} ion concentration among all groups, indicating possible Ca^{2+} release from the ZC21 alloy to the media. Intracellular Ca^{2+} released from BMSCs should not contribute much to the Ca^{2+} ion concentration in the media because the intracellular Ca concentrations for most cells are in the range of 0.1–1 μM,[58] which is much lower than the Ca levels of 1–3 mM in the culture media. The results in Figure 10c confirmed this, since no significant difference was found in Ca^{2+} ion concentrations between the cell-only and

media-only reference groups. Therefore, insoluble Ca-containing degradation products on the surface of ZC21, deposited from the media or originating from the ZC21 alloy, could be the main factor that promoted BMSC adhesion on ZC21 pins than on pure Mg pins under the direct contact conditions of both culture methods.

Soluble degradation products including OH^- ions and metallic ions, such as Mg^{2+}, Zn^{2+}, and Ca^{2+}, are the major factors that affect BMSC behaviors in indirect contact conditions. The pH values of the media, as well as the Mg^{2+}, Zn^{2+}, and Ca^{2+} ion concentrations, in the media of all groups in both culture methods of this study were well below cytotoxic values reported in literature.[28,53] Accordingly, BMSCs showed high viability under indirect contact conditions in both culture methods for all groups. As shown in Figure 9b, the pH values of all groups were around 8.4 in direct exposure culture and were around 8.0 for all groups in direct culture. Our previous study showed that BMSC viability reduced significantly at pH 9.5, but BMSCs showed no statistical difference in viability when the media pH was initially adjusted to 8–9.[28] Furthermore, the bicarbonate buffering system of DMEM, which is similar to the buffering system in the human body, could effectively mediate the alkalinity (transient pH < 9.0) back to normal conditions for cell culture.[28,59] Since our results showed that BMSCs remained viable on and around ZC21 pins in both culture methods, the local pH probably had little influence on cell viability. As for Mg^{2+} ions, attached and viable BMSCs with similar densities were observed after 24 h of culture in DMEM supplemented with 0–27.6 mM Mg^{2+} ion concentration in the previous study.[28] In this study, Mg^{2+} ion concentrations in all groups after 24 h culture were in the range of 0.7–3.0 mM, as shown in Figure 10a, which are in the cytocompatible range. ZC21 also released Zn^{2+} and Ca^{2+} ions during degradation, but the amounts of Zn^{2+} and Ca^{2+} ions released from ZC21 were much lower than that of Mg^{2+} ions, as Zn and Ca were alloying elements present in smaller amounts in the samples. More importantly, the measured 4–8 μMZn^{2+} and 1.5–2.6 mM Ca^{2+} ion concentrations for all groups in both culture methods in this study were well below their respective cytotoxic values reported in literature (60 μM for Zn and 30 mM for Ca).[60]

Cytocompatibility of ZSr41 alloys with BMSCs has been reported in our previous publications.[8,12] The behaviors of BMSCs in the direct culture with four as-rolled Mg-4Zn-*x*Sr alloys (x = 0.15, 0.5, 1.0, 1.5 wt %) were first studied, and the results showed that BMSCs exhibited higher viability on Mg-4Zn-1Sr (ZSr41) and Mg-4Zn-1.5Sr than Mg-4Zn-0.5Sr and Mg-4Zn-0.15Sr.[8] The as-rolled Mg–Zn–Sr alloy samples had a dimension of 5 mm × 5 mm × 1 mm. Collectively considering the properties of the four Mg-4Zn-xSr alloys, ZSr41 was chosen to be further studied as intramedullary pins in vitro with BMSCs and in vivo in rat tibia.[12] The as-drawn ZSr41 pins showed a general trend of increasing cell densities with increasing incubation time from 24 to 72 h, when they were cultured with BMSCs using the exposure culture method, which indicated cell proliferation over time.[12] The as-drawn ZSr41 pins showed a complete resorption time of 8 weeks and a significant net bone growth because of stimulatory effects of the metallic ions released, when they were implanted as intramedullary pins in rat tibia. Therefore, the same as-drawn ZSr41 pins as previously studied[12] were included in the bacterial culture with MRSA and implanted in the mouse femoral defect in vivo in this study for comparison. The ZSr41 alloy has been previously studied in BMSC culture,[8,12] but this was the first study to examine the

ZSr41 alloy in bacterial culture and in femoral defects, along with the ZC21 alloy of interest and pure Mg control.

The addition of Zn and Ca alloying elements in ZC21 improved the biocompatibility and degradation properties while reducing bacterial adhesion. The in vitro bacterial study demonstrated that MRSA adhesion significantly reduced on the surface of ZC21 when compared with ZSr41 and pure Mg. Moreover, ZC21 pins showed the strongest capacity for osteogenic induction and bone healing in a mouse femoral segmental defect in vivo. The X-ray images of mouse femur clearly showed that the ZC21 group induced bone growth and reduced the defect gap more than the ZSr41 group and pure Mg group. Overall, bioresorbable ZC21 alloy is promising for antimicrobial bone implant applications to reduce infections and eliminate the need of secondary surgeries for implant removal. Further in vivo studies on bone remodeling in an infection model using microcomputed tomography (microCT) and histological methods are necessary to fully elucidate the relationships between alloy degradation and the associated biological responses. Surface modifications or coatings could be applied onto the ZC21 alloy to further reduce the alloy degradation, while improving bone regeneration to meet the requirements for specific clinical applications.

4.2. Degradation Behaviors of ZC21 Pins in Vitro and in Vivo in Comparison with Controls.

The daily degradation rates, corrosion crack width and crack area ratio on the surface were quantified to compare the degradation behaviors of ZC21and Mg pins in vitro and in vivo. In the 24-h BMSC/DMEM culture system in vitro, the daily degradation rate of ZC21 was statistically faster than that of Mg in the direct exposure culture but was lower in the direct culture and no statistical difference was detected. However, for both culture methods, the crack width and crack area ratio on the surface of ZC21 were statistically smaller than Mg, indicating more desirable degradation mode. Larger corrosion cracks on Mg might cause severe corrosion in the longer term than 24 h and might release larger pieces of degradation products, which could cause catastrophic failure later. Even though ZC21 showed higher degradation rate than Mg in 24-h direct exposure culture, the degradation mode of ZC21 may lead to more uniform and slower degradation in the longer term in vivo. Indeed, after 12 weeks of implantation in mouse femoral defect model, ZC21 pins still largely retained their shape but Mg pins were completely degraded, confirming that ZC21 pins degraded much slower than Mg pins in vivo.

Intrinsic properties such as the composition, microstructure, processing conditions, dimension, geometry, and surface conditions of samples are the key factors that could affect the degradation behaviors of Mg-based materials. However, the effects of these material factors on sample degradation are manifested differently when coupled with different environmental conditions present in vitro and in vivo. The cells, proteins, and ions in the in vitro BMSC/DMEM culture system could affect the degradation behaviors of Mg-based materials. Interestingly, ZC21 showed a higher daily degradation rate, coupled with a greater crack width and crack area ratio in the direct exposure culture than in the direct culture, suggesting different culture methods did affect its in vitro degradation behaviors. Furthermore, in the direct exposure culture, cells that had already been established for 24 h

before the introduction of ZC21 pins could release acidic metabolites into the media. The presence of pre-established cells and acidic metabolites prior to introduction of the sample pins appeared to affect the degradation of ZC21 more than that of pure Mg, as shown in Figure 10d–f.

The in vivo environment is more dynamic and complex than in vitro culture systems, and more factors, such as the selection of different animal models, the location of implantation, and the conditions of fluid flow and loading at the implantation sites, could affect the in vivo degradation of Mg-based materials. For example, the addition of Zn as an alloying element could improve tensile and creep strength[32] and enhance the corrosion resistance of Mg alloys. However, such benefits may not be clearly shown in the in vitro culture systems because of the relatively static environment, lack of mechanical stress, and short culture duration. In contrast, the beneficial roles of Zn and Ca alloying elements on Mg-based materials were clearly expressed in the in vivo system used here because of the dynamic environment with systemic fluid flow and mechanical stress. ZC21 demonstrated significantly better degradation performance than pure Mg after 12 weeks of implantation in vivo. In this study, the ZSr41 control pins also partially retained their shape and had a slower degradation rate than Mg pins after 12 weeks of implantation in a mouse femoral defect. In a previous study, ZSr41 pins had a significantly faster degradation rate than pure Mg pins in a rat tibia model during in vivo implantation for 47 days.[12] The difference in the degradation behaviors of ZSr41 pins in these two studies was most likely caused by the differences in the animal models (segmental defect in a mouse femur versus medullary cavity in a rat tibia), and different fluid flow and loading conditions at the two different implantation sites.

Finally, the average daily degradation rates of ZC21, ZSr41, and Mg pins in vitro and in vivo from this study were compared with the values from the previous in vitro and in vivo studies, and the results are summarized in Figure 16. It is important to pay attention to all the key parameters included in Figure 16 that could affect the degradation results, including sample dimension, different processing parameters, and experimental conditions, such as medium type and animal model, even when the alloy composition is the same. When the experimental conditions varied, the calculated average daily degradation rates of the alloys that had the same composition might be different. Specifically, the results from the following studies were compared with the degradation results of this study: the average daily degradation rates of ZC21 and Mg sheets in the direct culture (abbreviated as D) with BMSCs in DMEM media (averaged from 3 days),[28] ZSr41 and Mg intramedullary pins in rat tibia (averaged from 47 days),[12] ZSr41 and Mg pins in exposure culture (abbreviated as E, that is, samples were placed in Transwell inserts in the culture well with BMSCs in DMEM media) that were averaged from 3 days,[12] and the average daily degradation rates of ZSr41 and Mg sheets in direct culture (D) with BMSCs in DMEM media (averaged from 3 days).[8] The comparison in Figure 16 demonstrated that the degradation rates of ZC21, ZSr41, and Mg varied dramatically under different experimental conditions in vitro and in vivo. In addition to the alloy composition, material factors, such as processing conditions, sample geometry, and sample dimension, as well as environmental factors associated with the differences between in vitro culture methods and in vivo models, could influence the degradation behaviors of the samples, which should be carefully considered when comparing the degradation behaviors in vitro and in vivo. ZC21 showed similar degradation

rates in the direct culture and direct exposure culture with BMSCs in DMEM because of the same sample dimension, the same type of culture media and the same volume of culture media. However, the degradation rate of ZC21 increased dramatically in the culture with MRSA in rSBF+FBS in comparison with the BMSC+DMEM culture system, likely because of the differences in the sample size (5mmlength versus 15 mm length), the culture media (rSBF+FBS versus DMEM), and the volume of culture media (0.75 mL versus 3 mL). The degradation rate of ZC21 in vivo was close to that in the BMSC+DMEM culture system. Overall, the in vitro cell culture systems with relevant cell and media types could simulate certain in vivo physiological conditions with the presence of relevant ions, proteins and cells, which is useful for initial screening studies of Mg-based materials, but in vivo studies in relevant animal models are still necessary.

5. CONCLUSION

This article reported for the first time the cytocompatibility and in vitro degradation of ZC21 pins in the direct exposure culture and direct culture, the antibacterial activities of ZC21 against MRSA bacteria, and the in vivo degradation and osteogenic potential of ZC21 pins in a mouse femoral defect model in a comparison study with ZSr41 alloy and pure Mg. The BMSC adhesion density on ZC21 pins was significantly higher than on Mg pins in both in vitro culture methods; the cell adhesion density around ZC21 pins was similar to the cell-only positive control in both in vitro culture methods, which confirmed that ZC21 is cytocompatible with BMSCs. The ZC21 pins showed fewer corrosion cracks on the surface than Mg pins after 24-h in vitro culture, and significantly slower degradation than pure Mg pins after 12 weeks of in vivo implantation. ZC21 surface showed more significant antibacterial properties than ZSr41 and Mg in the 24-h culture with MRSA. Furthermore, the ZC21 group demonstrated the most promising bone healing in mouse femoral defects when compared with ZSr41 alloy and Mg pins after 12 weeks of in vivo implantation. Thus, ZC21 alloy should be further studied toward clinical translation for biodegradable implant applications.

ACKNOWLEDGMENTS

The authors would like to acknowledge financial support from the U.S. National Institutes of Health (NIAMS award 1R03AR069373), U.S. National Science Foundation (CBET award 1512764, 1125801), Burroughs Wellcome Fund (1011235), Hellman Faculty Fellowship (H.L.), and the University of California (UC) Regents Faculty Development Award (H.L.). The authors thank the Central Facility for Advanced Microscopy and Microanalysis (CFAMM) at the University of California at Riverside (UCR) for access to the SEM and EDS. The authors thank the California Alliance for Minority Participation (CAMP) program and Materials Connection (MaCREU) program (NSF DMR award 1359136) at the UCR for supporting the undergraduate student researcher (E.V.). The authors also thank Neema Masoudipour and Lijing Yang for helping with cell culture. The content is solely the responsibility of the authors and does not represent the official views of the National Institutes of Health or the National Science Foundation.

REFERENCES

(1). Staiger MP; Pietak AM; Huadmai J; Dias G Magnesium and its alloys as orthopedic biomaterials: a review. Biomaterials 2006, 27 (9), 1728–1734. [PubMed: 16246414]

(2). Witte F; Hort N; Vogt C; Cohen S; Kainer KU; Willumeit R; Feyerabend F Degradable biomaterials based on magnesium corrosion. Curr. Opin. Solid State Mater. Sci. 2008, 12 (5–6), 63–72.

(3). Cipriano AF; Guan R-G; Cui T; Zhao Z-Y; Garcia S; Johnson I; Liu H; Ieee. In vitro Degradation and Cytocompatibility of Magnesium-Zinc-Strontium Alloys with Human Embryonic Stem Cells. 2012 Annual International Conference of the IEEE Engineering in Medicine and Biology Society 2012, 2432–2435.

(4). Waizy H; Seitz J-M; Reifenrath J; Weizbauer A; Bach F-W; Meyer-Lindenberg A; Denkena B; Windhagen H Biodegradable magnesium implants for orthopedic applications. J. Mater. Sci. 2013, 48 (1), 39–50.

(5). Guan R-G; Cipriano AF; Zhao Z.-y.; Lock J; Tie D; Zhao T; Cui T; Liu H Development and evaluation of a magnesium-zinc-strontium alloy for biomedical applications - Alloy processing, microstructure, mechanical properties, and biodegradation. Mater. Sci. Eng., C 2013, 33 (7), 3661–3669.

(6). Zhao DW; Witte F; Lu FQ; Wang JL; Li JL; Qin L Current status on clinical applications of magnesium-based orthopaedic implants: A review from clinical translational perspective. Biomaterials 2017, 112, 287–302. [PubMed: 27770632]

(7). Peron M; Torgersen J; Berto F Mg and Its Alloys for Biomedical Applications: Exploring Corrosion and Its Interplay with Mechanical Failure. Metals 2017, 7 (7), 252.

(8). Cipriano AF; Sallee A; Guan RG; Lin A; Liu HN A Comparison Study on the Degradation and Cytocompatibility of Mg-4Zn-xSr Alloys in Direct Culture. ACS Biomater. Sci. Eng. 2017, 3 (4), 540–550. [PubMed: 33429621]

(9). Sanchez AHM; Luthringer BJC; Feyerabend F; Willumeit R Mg and Mg alloys: How comparable are in vitro and in vivo corrosion rates? A review. Acta Biomater. 2015, 13, 16–31. [PubMed: 25484334]

(10). Wang XJ; Xu DK; Wu RZ; Chen XB; Peng QM; Jin L; Xin YC; Zhang ZQ; Liu Y; Chen XH; Chen G; Deng KK; Wang HY What is going on in magnesium alloys? J. Mater. Sci. Technol. 2018, 34, 245.

(11). Zhang C; Driver N; Tian Q; Jiang W; Liu H Electrochemical deposition of conductive polymers onto magnesium microwires for neural electrode applications. J. Biomed. Mater. Res., Part A 2018, 106 (7), 1887–1895.

(12). Cipriano AF; Lin J; Lin A; Sallee A; Le B; Cortez Alcaraz MC; Guan R-G; Botimer G; Inceoglu S; Liu H Degradation of Bioresorbable Mg-4Zn-1Sr Intramedullary Pins and Associated Biological Responses in Vitro and in Vivo. ACS Appl. Mater. Interfaces 2017, 9 (51), 44332–44355. [PubMed: 29239597]

(13). Narita K; Tian Q; Johnson I; Zhang C; Kobayashi E; Liu H Degradation behaviors and cytocompatibility of Mg/β-tricalcium phosphate composites produced by spark plasma sintering. J. Biomed. Mater. Res., Part B 2019, 107, 2238–2253.

(14). Zheng YF; Gu XN; Witte F Biodegradable metals. Mater. Sci. Eng., R 2014, 77, 1–34.

(15). Tian QM; Zhang CX; Deo M; Rivera-Castaneda L; Masoudipour N; Guan RG; Liu HN Responses of human urothelial cells to magnesium-zinc-strontium alloys and associated insoluble degradation products for urological stent applications. Mater. Sci. Eng., C 2019, 96, 248–262.

(16). Ding YF; Wen CE; Hodgson P; Li YC Effects of alloying elements on the corrosion behavior and biocompatibility of biodegradable magnesium alloys: a review. J. Mater. Chem. B 2014, 2 (14), 1912–1933. [PubMed: 32261628]

(17). Zhang CX; Lin JJ; Liu HN Magnesium-based Biodegradable Materials for Biomedical Applications. MRS Adv. 2018, 3 (40), 2359–2364.

(18). El-Rahman S Neuropathology of aluminum toxicity in rats (glutamate and GABA impairment). Pharmacol. Res. 2003, 47 (3), 189–194. [PubMed: 12591013]

(19). Liu L; Li N; Lei T; Li K; Zhang Y The in vitro biological properties of Mg-Zn-Sr alloy and superiority for preparation of biodegradable intestinal anastomosis rings. Med. Sci. Monit. 2014, 20, 1056–1066. [PubMed: 24957079]

(20). Li H; Peng Q; Li X; Li K; Han Z; Fang D Microstructures, mechanical and cytocompatibility of degradable Mg-Zn based orthopedic biomaterials. Mater. Eng. 2014, 58, 43–51.

(21). Jeong Y; Kim W Enhancement of mechanical properties and corrosion resistance of Mg–Ca alloys through microstructural refinement by indirect extrusion. Corros. Sci. 2014, 82, 392–403.

(22). Cho SY; Chae S-W; Choi KW; Seok HK; Kim YC; Jung JY; Yang SJ; Kwon GJ; Kim JT; Assad M Biocompatibility and strength retention of biodegradable Mg-Ca-Zn alloy bone implants. J. Biomed. Mater. Res., Part B 2013, 101B (2), 201–212.

(23). Wang B; Gao J; Wang L; Zhu S; Guan S Biocorrosion of coated Mg-Zn-Ca alloy under constant compressive stress close to that of human tibia. Mater. Lett. 2012, 70, 174–176.

(24). Brar HS; Wong J; Manuel MV Investigation of the mechanical and degradation properties of Mg-Sr and Mg-Zn-Sr alloys for use as potential biodegradable implant materials. Journal of the Mechanical Behavior of Biomedical Materials 2012, 7, 87–95. [PubMed: 22340688]

(25). Bakhsheshi-Rad HR; Abdul-Kadir MR; Idris MH; Farahany S Relationship between the corrosion behavior and the thermal characteristics and microstructure of Mg-0.5Ca-xZn alloys. Corros. Sci. 2012, 64, 184–197.

(26). Zhang B; Hou Y; Wang X; Wang Y; Geng L Mechanical properties, degradation performance and cytotoxicity of Mg-Zn-Ca biomedical alloys with different compositions. Mater. Sci. Eng., C 2011, 31 (8), 1667–1673.

(27). Xu Z; Smith C; Chen S; Sankar J Development and microstructural characterizations of Mg-Zn-Ca alloys for biomedical applications. Mater. Sci. Eng., B 2011, 176 (20), 1660–1665.

(28). Cipriano AF; Sallee A; Guan RG; Zhao ZY; Tayoba M; Sanchez J; Liu HN Investigation of magnesium-zinc-calcium alloys and bone marrow derived mesenchymal stem cell response in direct culture. Acta Biomater. 2015, 12, 298–321. [PubMed: 25449917]

(29). Jiang W; Cipriano AF; Tian Q; Zhang C; Lopez M; Sallee A; Lin A; Cortez Alcaraz MC; Wu Y; Zheng Y; Liu H In vitro evaluation of MgSr and MgCaSr alloys via direct culture with bone marrow derived mesenchymal stem cells. Acta Biomater. 2018, 72, 407–423. [PubMed: 29626698]

(30). Coleman JE Zinc Proteins - Enzymes, Storage Proteins, Transcription Factors, and Replication Proteins. Annu. Rev. Biochem. 1992, 61, 897–946. [PubMed: 1497326]

(31). Farahany S; Bakhsheshi-Rad HR; Idris MH; Abdul Kadir MR; Lotfabadi AF; Ourdjini A In-situ thermal analysis and macroscopical characterization of Mg-xCa and Mg-0.5Ca-xZn alloy systems. Thermochim. Acta 2012, 527, 180–189.

(32). Boehlert CJ; Knittel K The microstructure, tensile properties, and creep behavior of Mg-Zn alloys containing 0–4.4 wt.% Zn. Mater. Sci. Eng., A 2006, 417 (1–2), 315–321.

(33). Zhang BP; Wang Y; Geng L Research on Mg-Zn-Ca Alloy as Degradable Biomaterial. Biomaterials - Physics and Chemistry 2011, 183–204.

(34). Rosalbino F; De Negri S; Saccone A; Angelini E; Delfino S Bio-corrosion characterization of Mg-Zn-X (X = Ca, Mn, Si) alloys for biomedical applications. J. Mater. Sci.: Mater. Med. 2010, 21 (4), 1091–1098. [PubMed: 20020186]

(35). Sun Y; Zhang B; Wang Y; Geng L; Jiao X Preparation and characterization of a new biomedical Mg-Zn-Ca alloy. Mater. Design 2012, 34, 58–64.

(36). Yin P; Li NF; Lei T; Liu L; Ouyang C Effects of Ca on microstructure, mechanical and corrosion properties and biocompatibility of Mg-Zn-Ca alloys. J. Mater. Sci.: Mater. Med. 2013, 24 (6), 1365–1373. [PubMed: 23608999]

(37). Zhang E; Yang L Microstructure, mechanical properties and bio-corrosion properties of Mg-Zn-Mn-Ca alloy for biomedical application. Mater. Sci. Eng., A 2008, 497 (1–2), 111–118.

(38). Li YC; Li MH; Hu WY; Hodgson P; Wen C Biodegradable Mg-Ca and Mg-Ca-Y alloys for Regenerative Medicine. Mater. Sci. Forum 2010, 654–656, 2192–2195.

(39). Li ZJ; Gu XN; Lou SQ; Zheng YF The development of binary Mg-Ca alloys for use as biodegradable materials within bone. Biomaterials 2008, 29 (10), 1329–1344. [PubMed: 18191191]

(40). Tian QM; Deo M; Rivera-Castaneda L; Liu HN Cytocompatibility of Magnesium Alloys with Human Urothelial Cells: A Comparison of Three Culture Methodologies. ACS Biomater. Sci. Eng. 2016, 2 (9), 1559–1571. [PubMed: 33440591]

(41). Pan YK; He SY; Wang DG; Huang DL; Zheng TT; Wang SQ; Dong P; Chen CZ In vitro degradation and electrochemical corrosion evaluations of microarc oxidized pure Mg, Mg-Ca and Mg-Ca-Zn alloys for biomedical applications. Mater. Sci. Eng., C 2015, 47, 85–96.

(42). Lu Y; Bradshaw AR; Chiu YL; Jones IP Effects of secondary phase and grain size on the corrosion of biodegradable Mg-Zn-Ca alloys. Mater. Sci. Eng., C 2015, 48, 480–486.

(43). Hofstetter J; Martinelli E; Pogatscher S; Schmutz P; Povoden-Karadeniz E; Weinberg AM; Uggowitzer PJ; Loffler JF Influence of trace impurities on the in vitro and in vivo degradation of biodegradable Mg-5Zn-0.3Ca alloys. Acta Biomater. 2015, 23, 347–353. [PubMed: 25983315]

(44). Ramya M; Sarwat SG; Udhayabanu V; Subramanian S; Raj B; Ravi KR Role of partially amorphous structure and alloying elements on the corrosion behavior of Mg-Zn-Ca bulk metallic glass for biomedical applications. Mater. Des. 2015, 86, 829–835.

(45). Lee J-W; Han H-S; Han K-J; Park J; Jeon H; Ok M-R; Seok H-K; Ahn J-P; Lee KE; Lee D-H; Yang S-J; Cho S-Y; Cha P-R; Kwon H; Nam T-H; Han JHL; Rho H-J; Lee K-S; Kim Y-C; Mantovani D Long-term clinical study and multiscale analysis of in vivo biodegradation mechanism of Mg alloy. Proc. Natl. Acad. Sci. U. S. A. 2016, 113 (3), 716–721. [PubMed: 26729859]

(46). Bian D; Zhou WR; Liu Y; Li N; Zheng YF; Sun ZL Fatigue behaviors of HP-Mg, Mg-Ca and Mg-Zn-Ca biodegradable metals in air and simulated body fluid. Acta Biomater. 2016, 41, 351–360. [PubMed: 27221795]

(47). Li H; Liu DB; Zhao Y; Jin F; Chen MF The Influence of Zn Content on the Corrosion and Wear Performance of Mg-Zn-Ca Alloy in Simulated Body Fluid. J. Mater. Eng. Perform. 2016, 25 (9), 3890–3895.

(48). Zhang CZ; Zhu SJ; Wang LG; Guo RM; Yue GC; Guan SK Microstructures and degradation mechanism in simulated body fluid of biomedical Mg-Zn-Ca alloy processed by high pressure torsion. Mater. Des. 2016, 96, 54–62.

(49). Roche V; Koga GY; Matias TB; Kiminami CS; Bolfarini C; Botta WJ; Nogueira RP; Jorge AM Jr. Degradation of biodegradable implants: The influence of microstructure and composition of Mg-Zn-Ca alloys. J. Alloys Compd. 2019, 774, 168–181.

(50). Gu XN; Wang F; Xie XH; Zheng MY; Li P; Zheng YF; Qin L; Fan YB In vitro and in vivo studies on as-extruded Mg-5.25 wt.% Zn-0.6wt.% Ca alloy as biodegradable metal. Sci. China Mater. 2018, 61 (4), 619–628.

(51). Cipriano AF; Sallee A; Tayoba M; Cortez Alcaraz MC; Lin A; Guan R-G; Zhao Z-Y; Liu H Cytocompatibility and early inflammatory response of human endothelial cells in direct culture with Mg-Zn-Sr alloys. Acta Biomater. 2017, 48, 499–520. [PubMed: 27746360]

(52). Guan RG; Cipriano AF; Zhao ZY; Lock J; Tie D; Zhao T; Cui T; Liu H Development and evaluation of a magnesium-zinc-strontium alloy for biomedical applications - Alloy processing, microstructure, mechanical properties, and biodegradation. Mater. Sci. Eng., C 2013, 33 (7), 3661–3669.

(53). Cipriano AF; Zhao T; Johnson I; Guan R-G; Garcia S; Liu H In vitro degradation of four magnesium-zinc-strontium alloys and their cytocompatibility with human embryonic stem cells. J. Mater. Sci.: Mater. Med. 2013, 24 (4), 989–1003. [PubMed: 23361966]

(54). Nguyen TY; Cipriano AF; Guan R-G; Zhao Z-Y; Liu H In vitro interactions of blood, platelet, and fibroblast with biodegradable magnesium-zinc-strontium alloys. J. Biomed. Mater. Res., Part A 2015, 103 (9), 2974–2986.

(55). Wetteland CL; Nguyen N-YT; Liu H Concentration-dependent behaviors of bone marrow derived mesenchymal stem cells and infectious bacteria toward magnesium oxide nanoparticles. Acta Biomater. 2016, 35, 341–356. [PubMed: 26923529]

(56). Gu X; Zheng Y; Cheng Y; Zhong S; Xi T In vitro corrosion and biocompatibility of binary magnesium alloys. Biomaterials 2009, 30 (4), 484–498. [PubMed: 19000636]

(57). Nguyen NYT; Grelling N; Wetteland CL; Rosario R; Liu H Antimicrobial Activities and Mechanisms of Magnesium Oxide Nanoparticles (nMgO) against Pathogenic Bacteria, Yeasts, and Biofilms. Sci. Rep. 2018, DOI: 10.1038/s41598-018-34567-5.

(58). Berridge MJ; Lipp P; Bootman MD The versatility and universality of calcium signalling. Nat. Rev. Mol. Cell Biol. 2000, 1 (1), 11–21. [PubMed: 11413485]

(59). Song G Control of biodegradation of biocompatable magnesium alloys. Corros. Sci. 2007, 49 (4), 1696–1701.

(60). Cha PR; Han HS; Yang GF; Kim YC; Hong KH; Lee SC; Jung JY; Ahn JP; Kim YY; Cho SY; Byun JY; Lee KS; Yang SJ; Seok HK Biodegradability engineering of biodegradable Mg alloys: Tailoring the electrochemical properties and microstructure of constituent phases. Sci. Rep. 2013, DOI: 10.1038/srep02367.

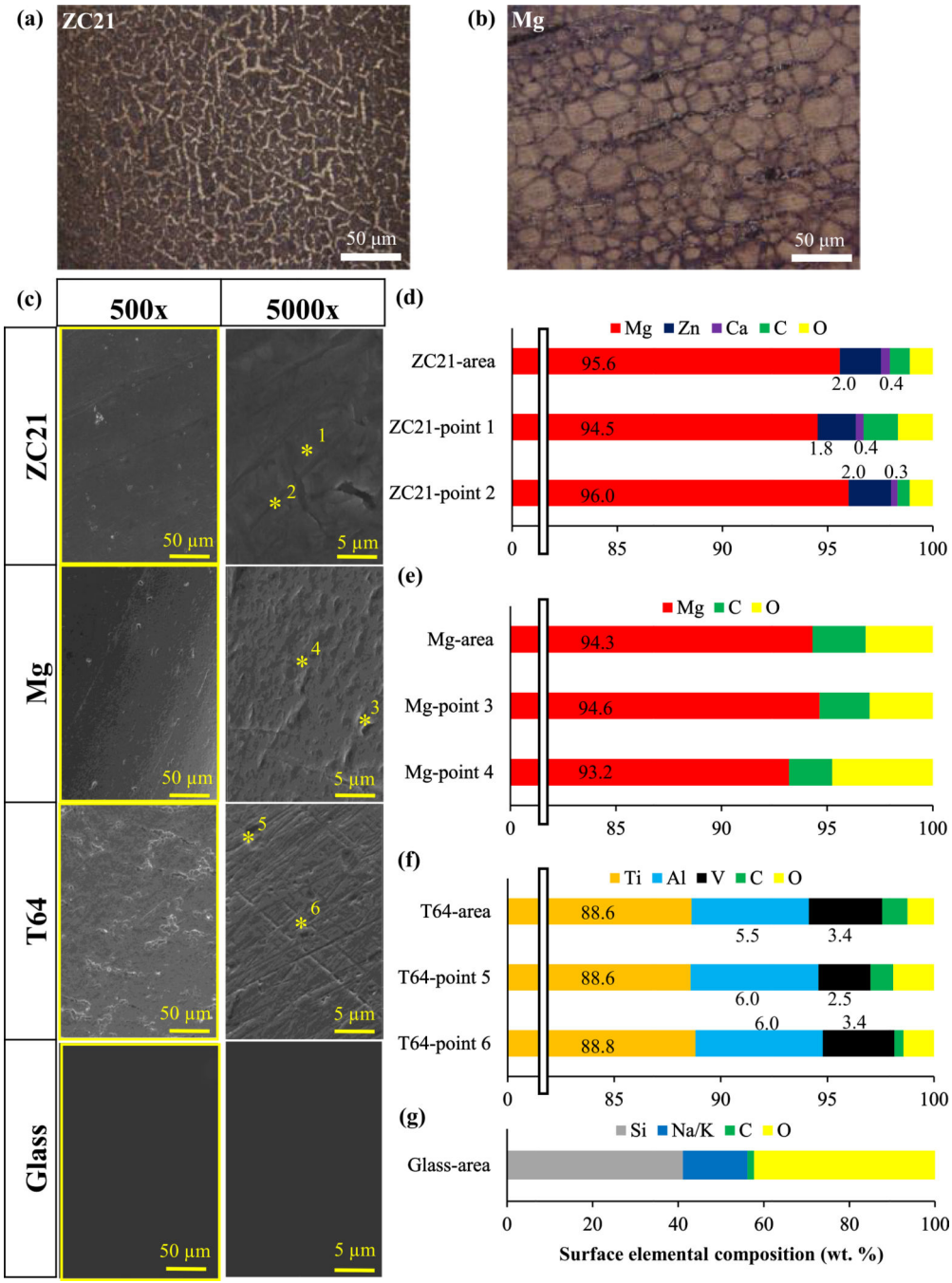

Figure 1.

Optical images for metallographic microstructures of (a) ZC21 and (b) Mg. (c–g) SEM images and EDS surface elemental composition (wt %) of ZC21, Mg, T64, and glass. (c) SEM images of the samples and controls at the 500× and 5000× original magnifications after polishing. (d) EDS area analysis (wt %) of ZC21 at 500× original magnification and EDS point analysis of point 1 and 2 in ZC21. (e) EDS area analysis (wt %) of Mg at 500× original magnification and EDS point analysis of point 3 and 4 in Mg. (f) EDS area analysis

(wt %) of T64 at 500× original magnification and EDS point analysis of point 5 and 6 in T64. (g) EDS area analysis (wt %) of glass at 500× original magnification.

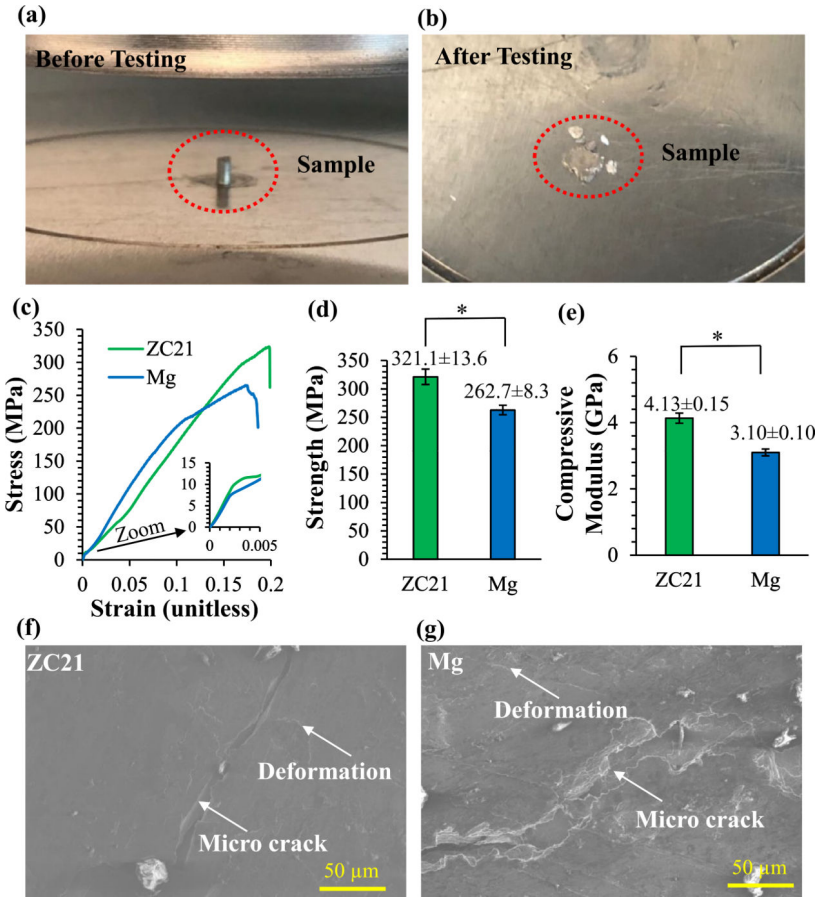

Figure 2.

Results of compression testing for ZC21 and Mg pins. (a, b) Representative photographs of a sample (a) before and (b) after compression testing. (c) Representative stress–strain curves of ZC21 and Mg pins. (d) The average ultimate compression strengths and (e) compressive moduli of ZC21 and Mg pins. (f, g) SEM images of the fracture surfaces of (f) ZC21 and (g) Mg at 500× original magnification after compression testing.

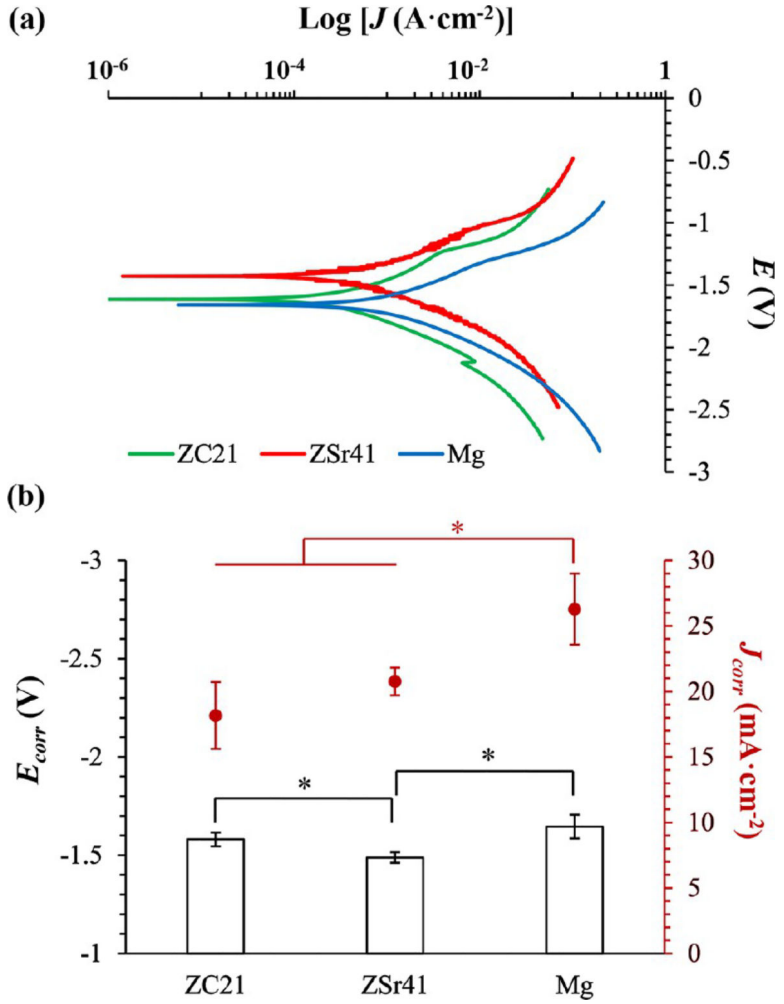

Figure 3.

Corrosion properties of the ZC21 pins and the control pins of ZSr41 and Mg from electrochemical testing in rSBF. (a) Representative potentiodynamic polarization (PDP) curves for ZC21, ZSr41, and Mg pins. (b) Corrosion potential and corrosion current density extrapolated from the PDP curves according to the Tafel method. The bar graphs with their axis on the left show the corrosion potential (E_{corr}), and the red dot symbols with their axis on the right show the corrosion current density (J_{corr}). Values are mean ± standard deviation ($n = 3$). *$p < 0.05$.

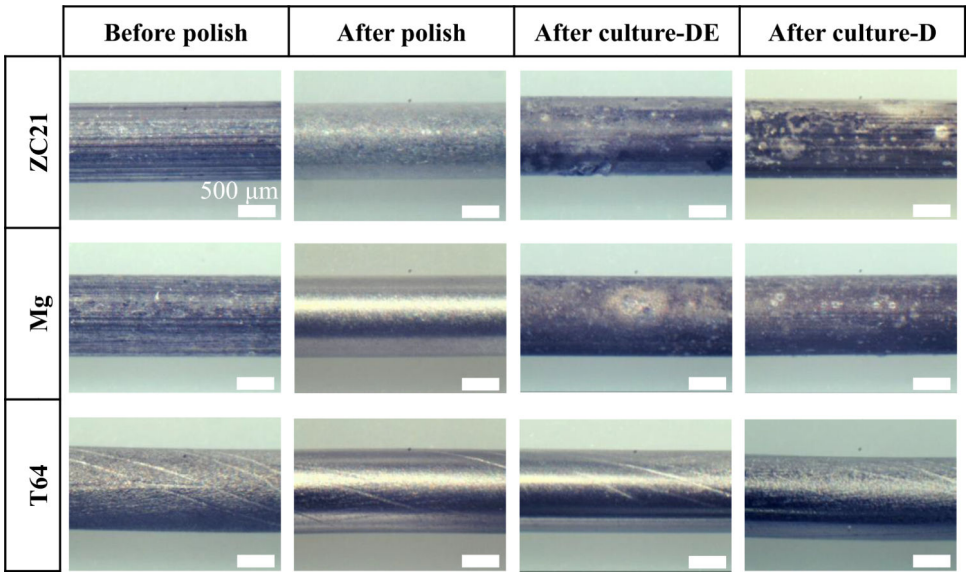

Figure 4.

Optical images of ZC21, Mg, and T64 before polishing, after polishing, after 24-h direct exposure culture (DE), and after 24-h direct culture (D) with BMSCs in DMEM. All samples were sequentially polished using the SiC papers of 600, 800, and 1200 grits. Scale bar = 500 μm for all images.

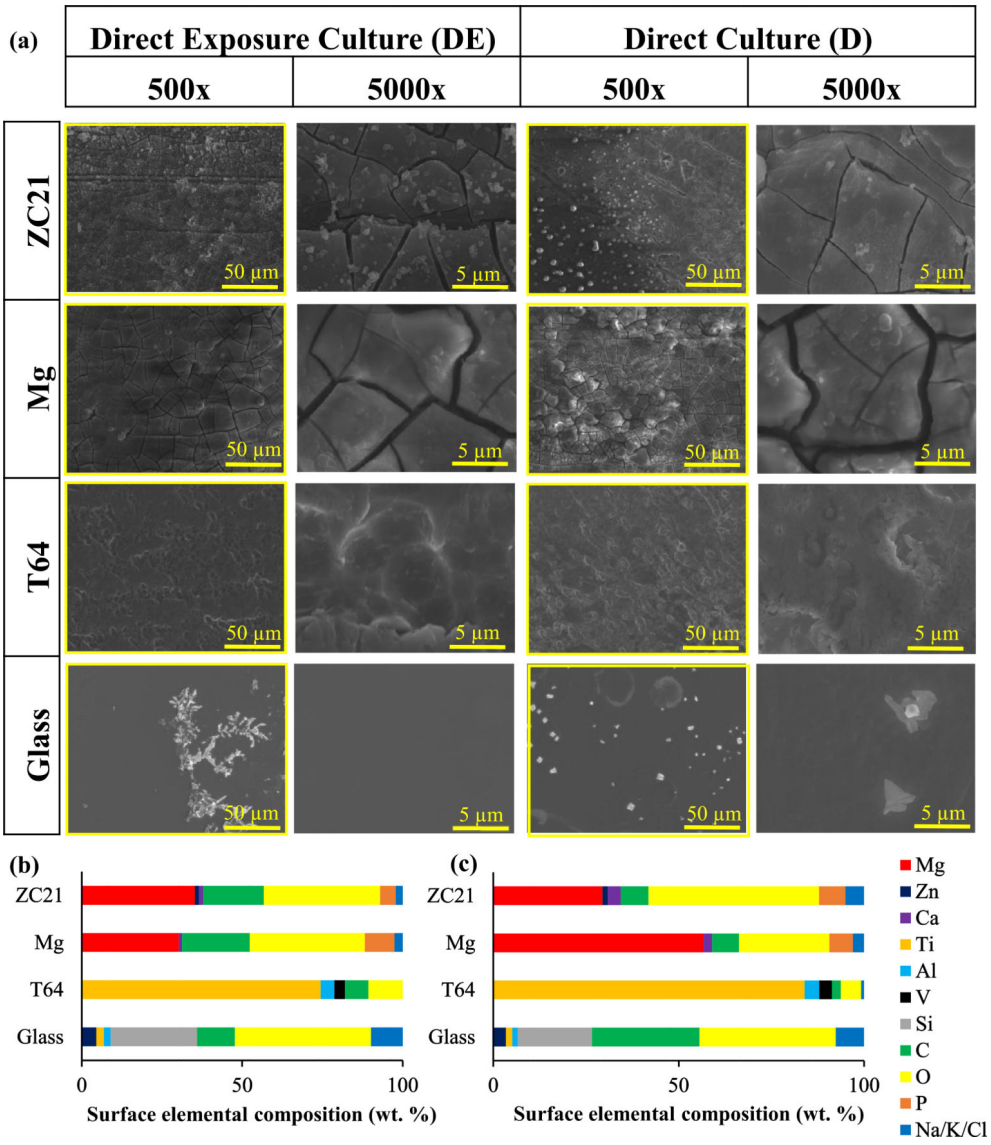

Figure 5.

SEM images and EDS analysis of ZC21, Mg, T64, and glass after 24-h direct exposure culture and direct culture with BMSCs in DMEM. (a) SEM images of all samples at 500× and 5000× original magnification after culture. (b) Surface elemental composition (wt %) of all samples at 500× original magnification after 24-h direct exposure culture. (c) Surface elemental composition (wt %) of all samples at 500× original magnification after 24-h direct culture.

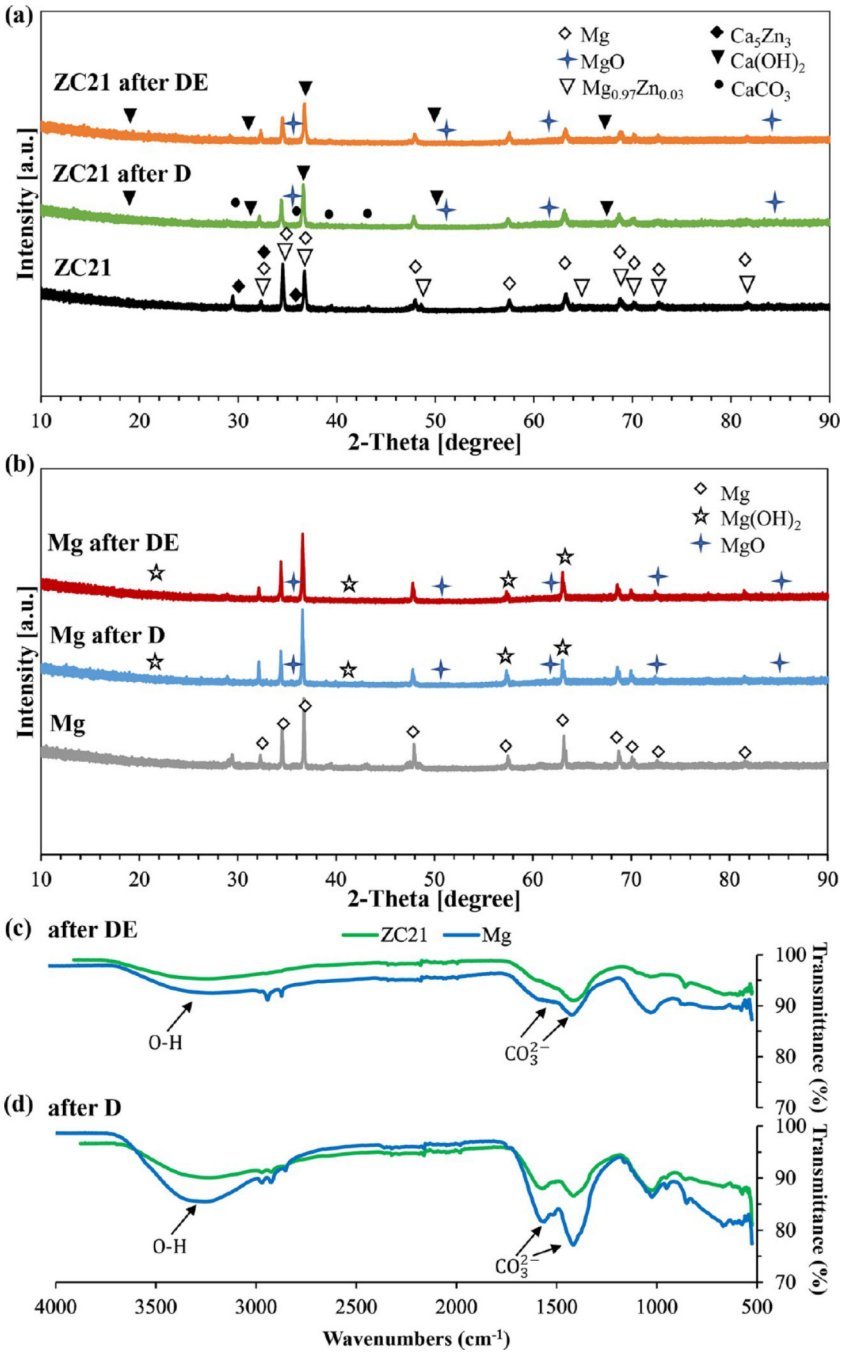

Figure 6.

XRD and FTIR spectra of ZC21 and Mg. (a) XRD spectra of ZC21 after 24-h direct exposure culture (DE), after 24-h direct culture (D), and before cell culture. Phases were identified based on Mg (ICSD pattern 01–089-7195), MgO (ICSD pattern 01–070-9183), $Mg_{0.97}Zn_{0.03}$ (ICSD pattern 01–071-9628), Ca_5Zn_3(ICSD pattern 01–073-8016), $Ca(OH)_2$(ICSD pattern 01–073-8394), and $CaCO_3$ (ICSD pattern 01–085-1108). (b) XRD spectra of Mg after 24-h DE, after 24-h D, and before cell culture. Phases were identified based on Mg (ICSD pattern 01–089-7195), MgO (ICSD pattern 01–070-9183) and

$Mg(OH)_2$(ICSD pattern 01–078-3960). (c) FTIR spectra of ZC21 and Mg after 24-h DE. (d) FTIR spectra of ZC21 and Mg after 24-h D.

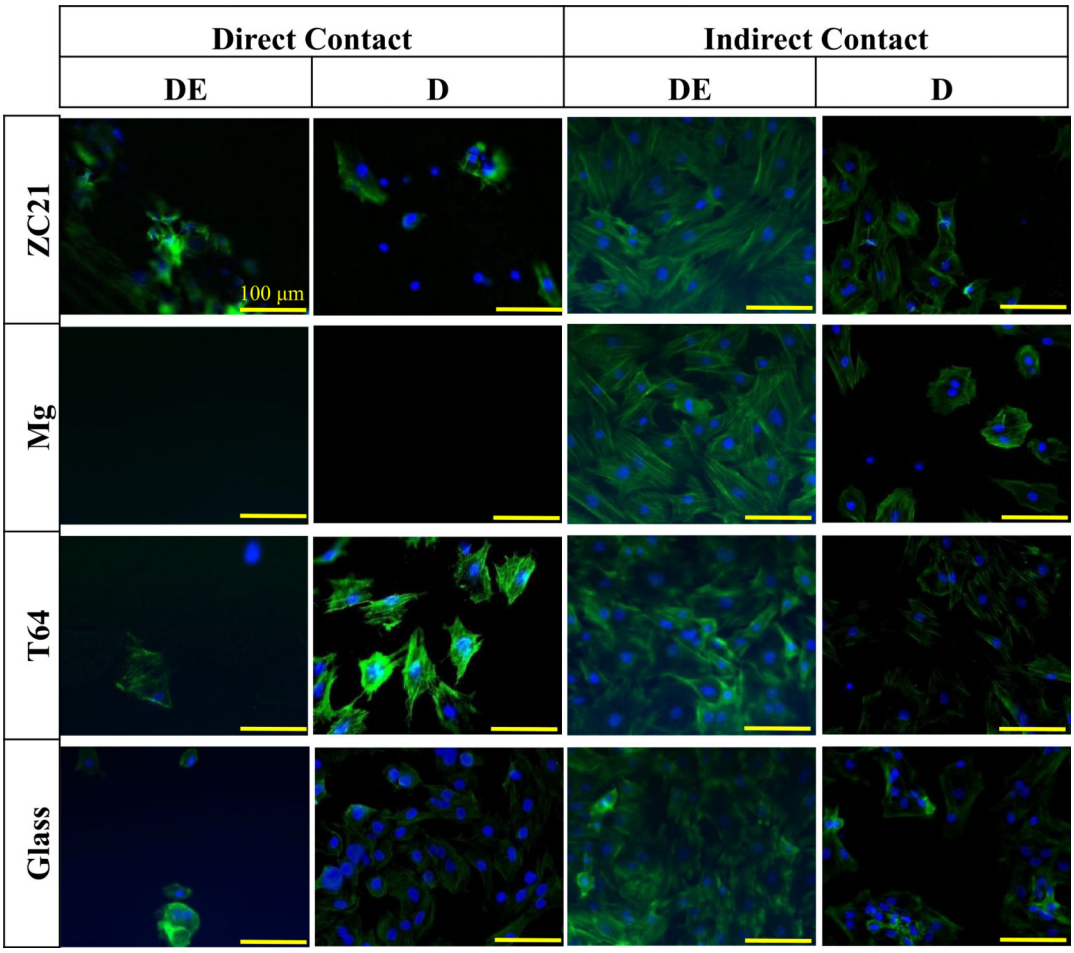

Figure 7.

Representative fluorescence images of BMSCs adhered on the sample surface (direct contact) and on the culture plate surrounding each corresponding sample (indirect contact) after 24-h direct exposure culture and 24-h direct culture with each group of materials of interest. Scale bar = 100 μm for all images.

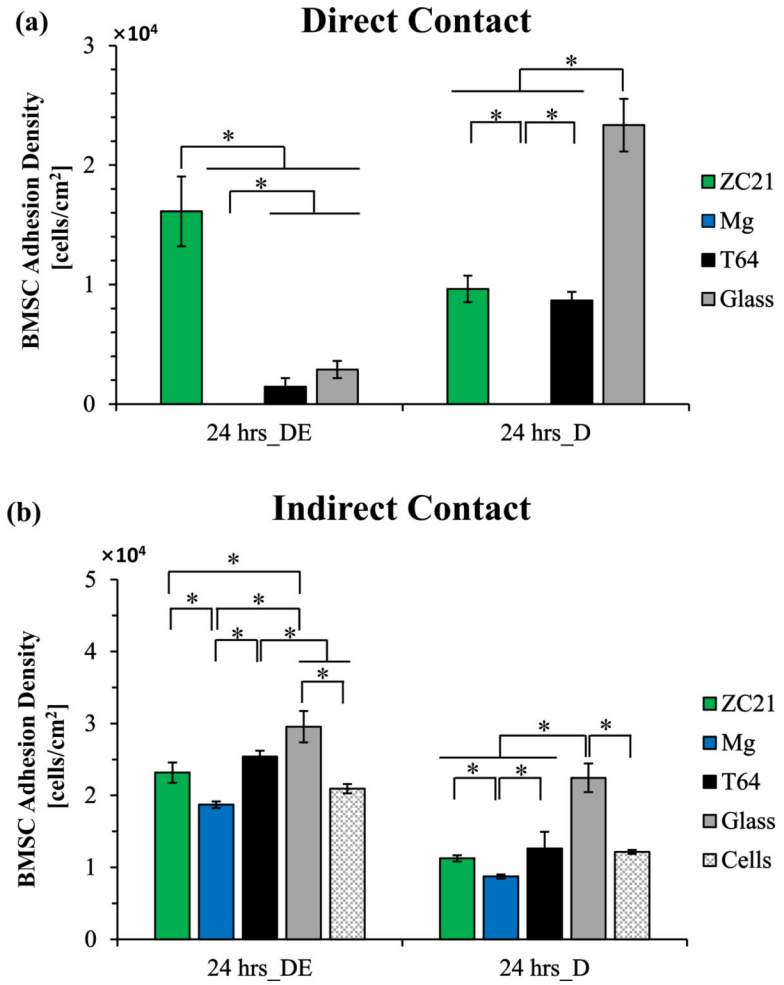

Figure 8.

BMSC adhesion density after 24-h direct exposure culture and 24-h direct culture on ZC21, pure Mg control, T64 control, glass reference and cell-only control on (a) the sample surface (direct contact), and (b) the culture plate surrounding each corresponding sample (indirect contact). Initial cell seeding density was 2×10^4 cells/cm^2. Values are mean ± standard error of the means, $n = 3$; $^*p < 0.05$.

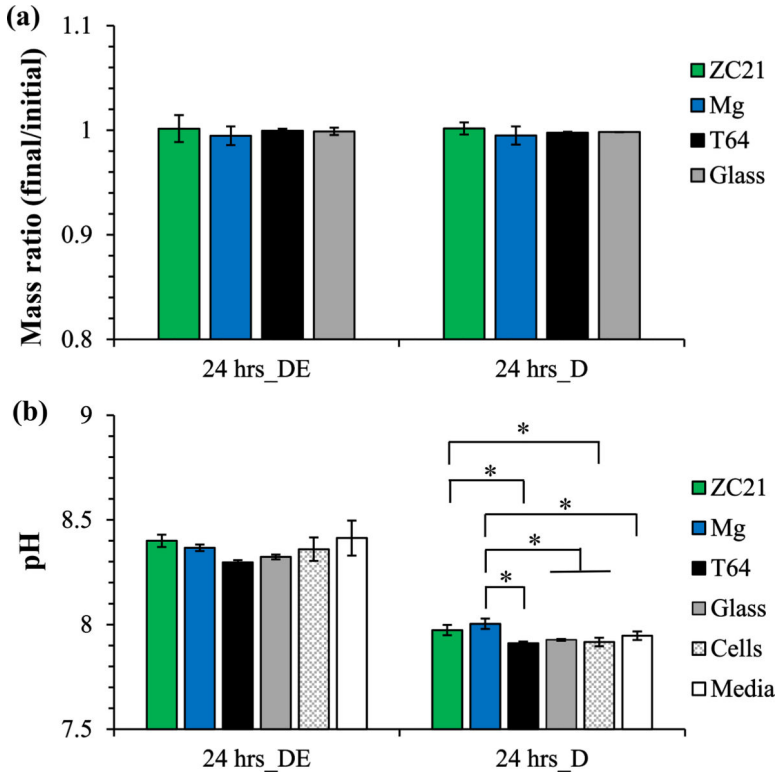

Figure 9.

(a) Mass change ratio (final/initial mass) of ZC21, pure Mg control, T64 control, and glass reference after 24-h direct exposure culture and 24-h direct culture; (b) pH values of the media collected from each well after 24-h direct exposure culture and 24-h direct culture. Data are expressed as mean ± standard deviation, $n = 3$; $^*p < 0.05$.

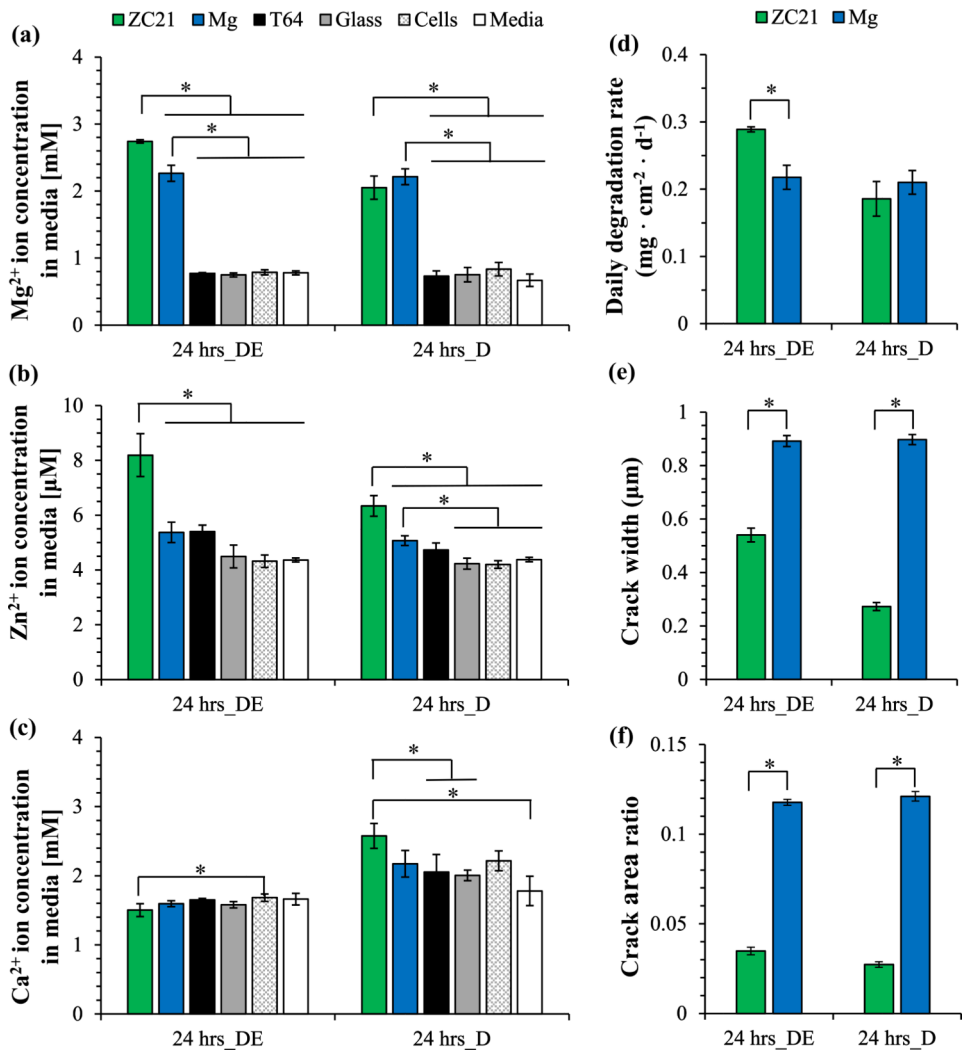

Figure 10.

Degradation of ZC21 and Mg pins in vitro after 24-h direct exposure culture (DE) and 24-h direct culture (D). (a–c) Ion concentration in the media collected from each well after 24-h DE and 24-h D: (a) Mg^{2+} ion concentration, (b) Zn^{2+} ion concentration, and (c) Ca^{2+} ion concentration. (d) The daily degradation rates of ZC21 and Mg after 24-h DE and D.(e) Crack width on the surface of ZC21 and Mg after 24-h DE and D. (f) Crack area ratio on the surface of ZC21 and Mg after 24-h DE and D. Data are mean ± standard deviation, $n = 3$; *$p < 0.05$.

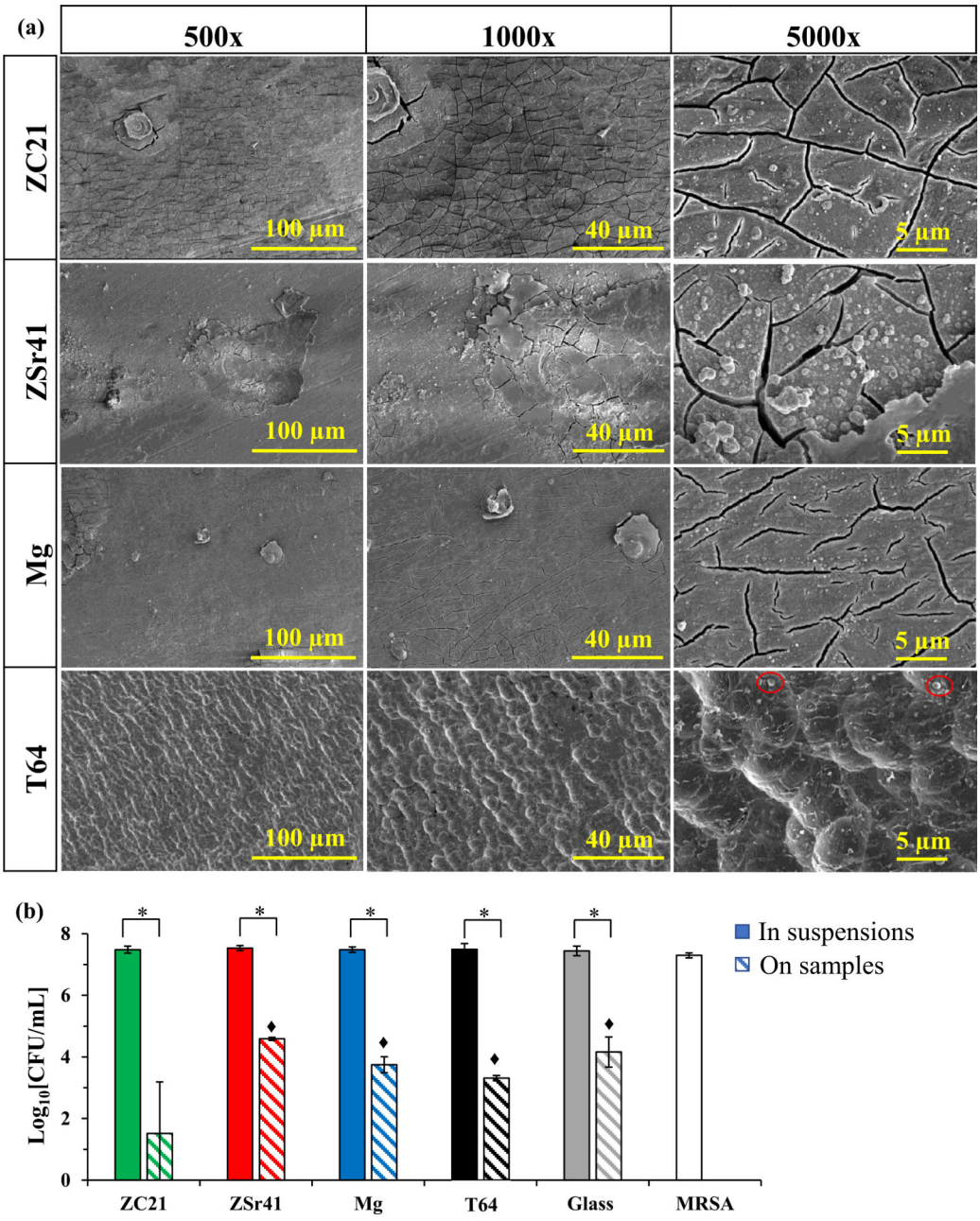

Figure 11.

(a) SEM images of ZC21, ZSr41, Mg, and T64 at the 500×, 1000×, and 5000× original magnifications after 24-h culture with methicillin-resistant *Staphylococcus aureus* (MRSA). Red circles were used to highlight bacteria on the sample surface. (b) Colony forming units (CFU) quantified for the viable MRSA after 24-h culture with the samples and controls. Data are mean ± standard deviation, $n = 3$; *$p < 0.05$. ♦$p < 0.05$ when compared with the CFU on ZC21 samples.

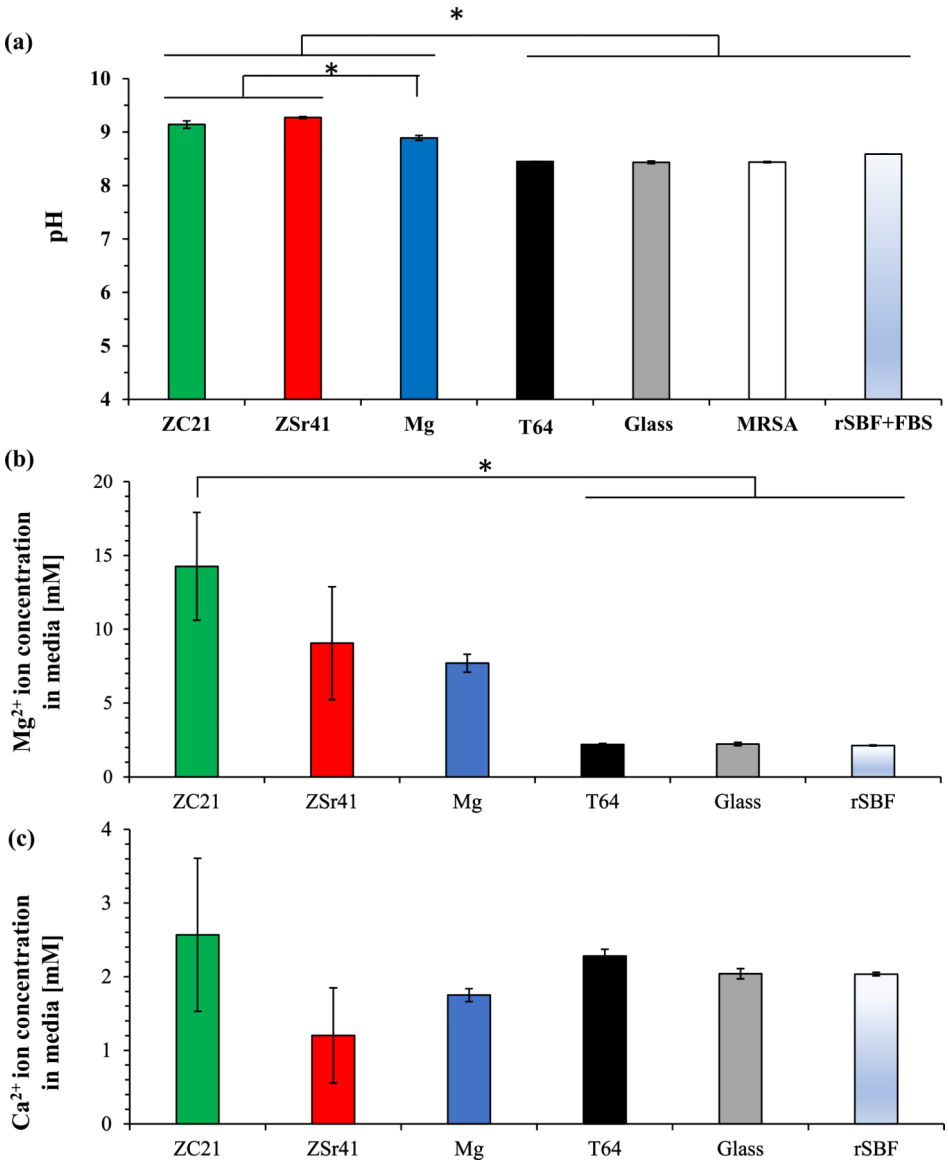

Figure 12.

Degradation of ZC21, ZSr41, and Mg pins in vitro after 24-h bacterial culture with MRSA. (a) pH values of the media collected from each well after 24-h MRSA culture. (b) Mg^{2+} ion concentration and (c) Ca^{2+} ion concentration in the media collected from each well after 24-h MRSA culture. Data are mean ± standard deviation, $n = 3$; $^{*}p < 0.05$.

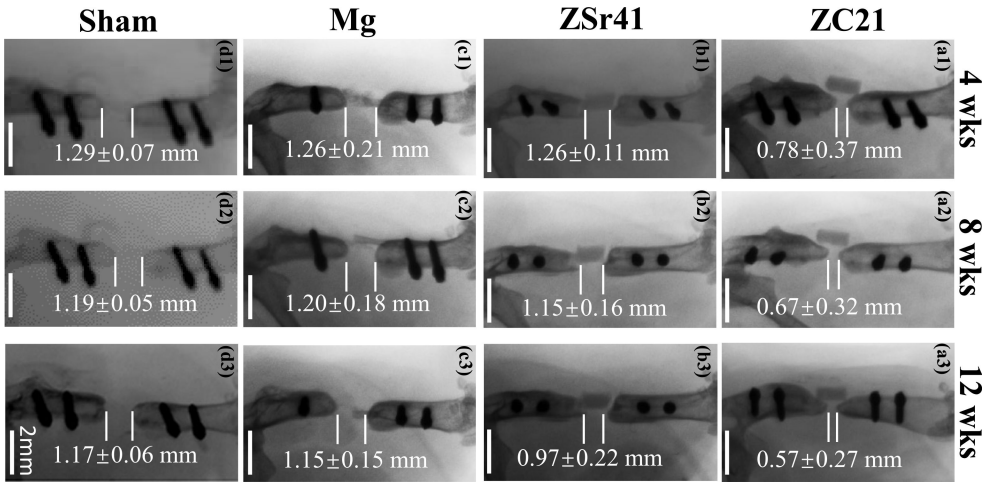

Figure 13.

Representative radiographs of a mouse femoral bone with a defect filled with ZC21 (a1–a3), ZSr41 (b1–b3), and Mg (c1–c3) at 4, 8, and 12 weeks after implantation. Sham designates the control group with a defect but no pin implant (d1–d3). The defect gap size at each time point is shown in each image; data are expressed as mean ± standard deviation. Scale bar = 2 mm for all radiographs.

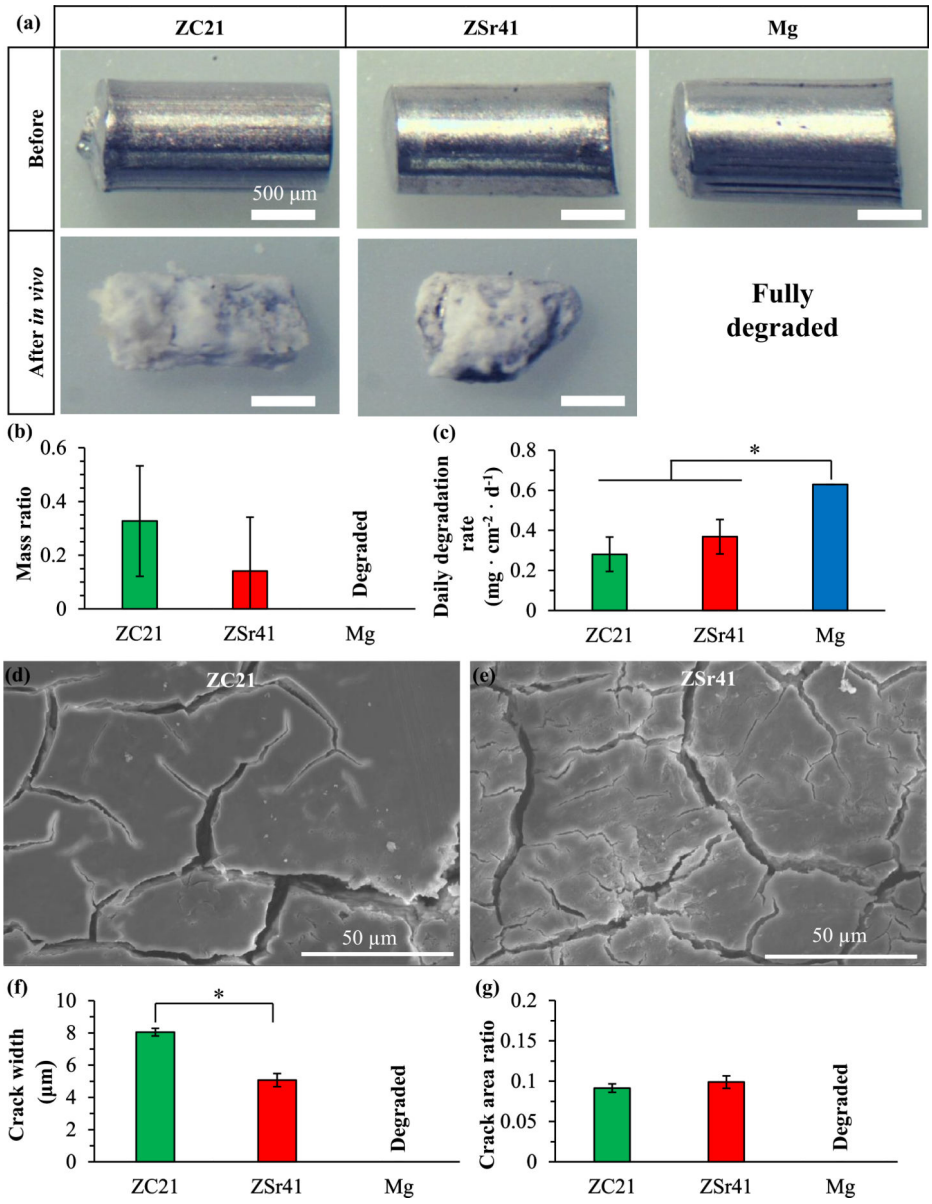

Figure 14.

Surface morphology, mass change, and degradation characterization of ZC21, ZSr41, and Mg before and after 12 weeks of in vivo implantation in mouse femoral defects. (a) Microscopic images of ZC21, ZSr41, and Mg before and after 12-week in vivo implantation. Scale bar = 500 μm for all images. (b) Mass ratio (final/initial mass) of ZC21, ZSr41, and Mg after 12-week in vivo implantation. (c) Daily degradation rate of ZC21, ZSr41, and Mg during 12-week in vivo implantation. (d) SEM image of ZC21 surface at an original magnification of 1000×. Image was taken on the surface region of ZC21 where the loose degradation layer was removed to identify crack width and area. (e) SEM image of ZSr41 surface at an original magnification of 1000×. Image was taken on the surface region of ZSr21, where the loose degradation layer was removed to identify crack width and area. (f) Crack width on the surface of ZC21 and ZSr41 after 12-week in vivo implantation. (f) Crack

area ratio on the surface of ZC21 and ZSr41 after 12-week in vivo implantation. Data are expressed as mean ± standard deviation, $n = 3$; $^{*}p < 0.05$.

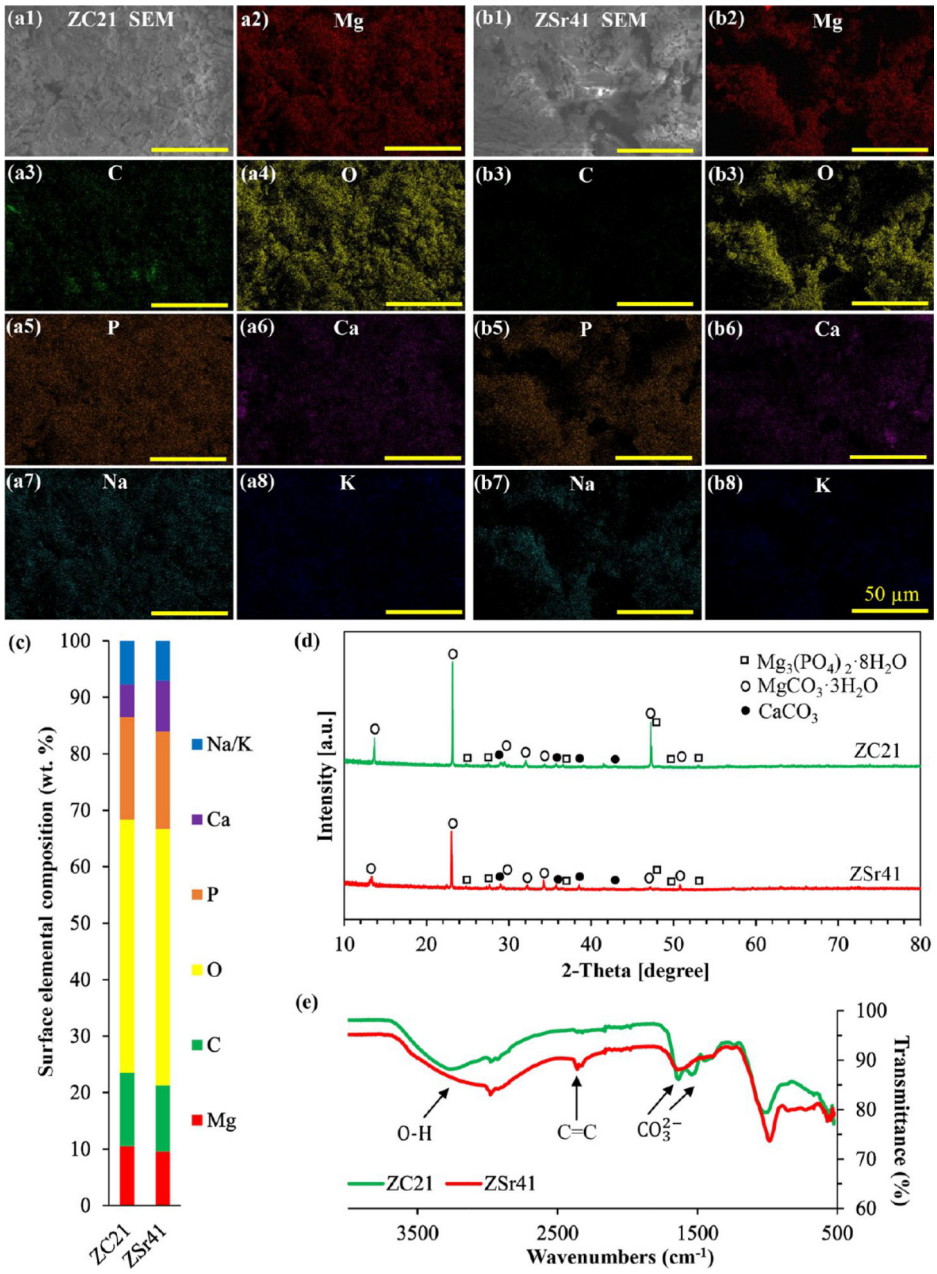

Figure 15.

Characterization of residual ZC21 and ZSr41 intramedullary pins dissected out after implantation in mouse femoral defects for 12 weeks. (a1–a8) SEM images of the deposition on ZC21 surface and corresponding surface elemental distribution maps (Mg, C, O, P, Ca, Na, and K). (b1–b8) SEM image of the deposition on ZSr41 surface and corresponding surface elemental distribution maps (Mg, C, O, P, Ca, Na, and K). (c) Surface elemental composition (wt %) quantified through EDS area analysis on SEM images of ZC21 and ZSr41 in (a1) and (b1).(d) XRD spectra of the surface of the residual ZC21 and ZSr41 intramedullary pins. (e) FTIR spectra of the surface of the residual ZC21 and ZSr41

intramedullary pins. Original magnification was 1000× and scale bar = 500 μm for all SEM images and EDS maps.

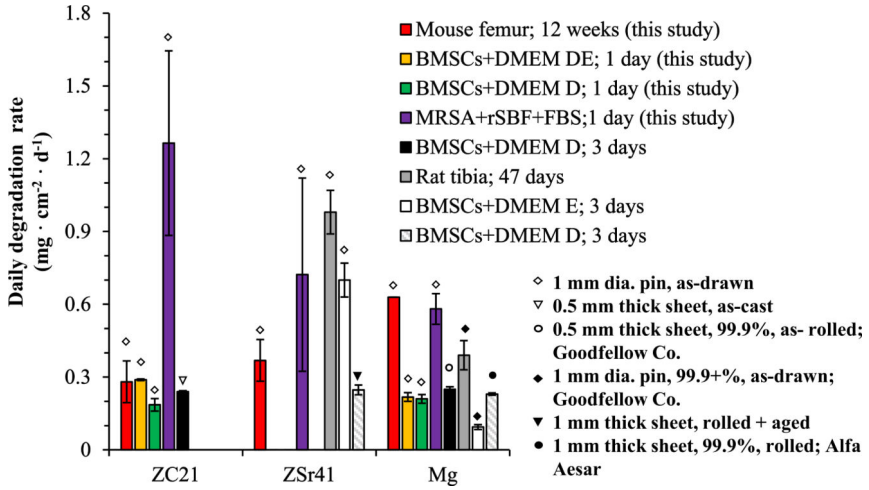

Figure 16.

Average daily degradation rates of ZC21, ZSr41, and Mg pins in vitro and in vivo from this study, in comparison with the daily degradation rates of these materials from previous studies.[8,12,28] The color and pattern of each bar designate the model system, that is, culture system, media type, culture method, and culture time for in vitro studies, and animal model type, anatomical location, and implantation time for in vivo studies. The icon above each bar designates the properties of respective samples (i.e., geometry, purity, and processing conditions for customized Mg and its alloys and the source for commercially procured pure Mg).

Table 1.

Development of Mg–Zn–Ca Ternary Alloys since 2014[41–50][a]

year	ref.	processing	Zn content	Ca content	focus	remarks
2014	41	as-cast	1.74 wt %	0.55 wt %	degradation in vitro	microarc oxidation (MAO) coating on the surface of Mg alloy
2014	42	as-cast	3 wt %	0.3 wt %	degradation in vitro	studied the effects of secondary phase and grain size on the corrosion
2015	28	as-cast	0.5, 1.0, 2.0, 4.0 wt %	0.5 wt %	degradation and cytocompatibility in vitro	the first report of in vitro cell responses at the dynamic interface and mechanisms
2015	43	extruded	5 wt %	0.3 wt %	degradation in vitro and in vivo	investigated the influence of trace impurities on degradation
2015	44	as-cast	30 at. % (52.5 wt %) Zn with 4 at.% (4.3 wt %) Ca; 35 at. % (58.0 wt %) Zn with 5 at. %(5.1 wt %) Ca		degradation in vitro	emphasized the role of partially amorphous structure and alloying elements on the corrosion behavior
2016	45	as-cast	1 wt %	5 wt %	degradation and biocompatibility in vivo	1-year clinical study and systematic investigation of bone formation mechanism
2016	46	extruded	2 wt %	0.2 wt %	fatigue behaviors	compared the fatigue behaviors in air and simulated body fluid
2016	47	extruded	3 and 4 wt %	0.2 wt %	degradation in vitro	investigated the influences of Zn content on the microstructure, mechanical properties, and corrosion and wear behavior
2016	48	extruded	2 wt %	0.24 wt %	degradation in vitro	processed by high pressure torsion to improve the corrosion resistance
2018	49	as-cast	31 at.% (53.6 wt %) Zn with 5 at.% (5.3 wt %) Ca; 24 at.% (45.0 wt %) Zn with 5 at.% (5.7 wt %) Ca		degradation in vitro	explained the influence of microstructure and composition on degradation
2018	50	extruded	5.25 wt %	0.6 wt %	biocompatibility in vitro and in vivo	compared in vitro and in vivo corrosion performance
2019	this study	as-drawn	2 wt %	0.5 wt %	degradation, antibaterial and biological performance in vitro and in vivo	systematically investigated the biocompatibility, mechanical properties, corrosion, degradation behavior and antibacterial properties of a promising Mg–Zn–Ca alloy for the first time

[a]Remarks summarize the key information of interest from the literature. Different Zn content and Ca content in Mg–Zn–Ca alloys are reviewed and listed in the table; the rest is Mg.